

# Constraints on oceanic meridional heat transport from combined measurements of oxygen and carbon

L. Resplandy · R. F. Keeling · B. B.  
Stephens · J. D. Bent · A. Jacobson ·  
C. Rödenbeck · S. Khatiwala

Received: date / Accepted: date

**Abstract** Despite its importance to the climate system, the ocean meridional heat transport is still poorly quantified. We identify a strong link between the northern hemisphere deficit in atmospheric potential oxygen ( $\text{APO} = \text{O}_2 + 1.1 \times \text{CO}_2$ ) and the ocean heat transport asymmetry between hemispheres, using atmospheric data and ocean interior inversions. Recent aircraft observations from the HIPPO campaign reveal a northern APO deficit in the tropospheric column of  $-10.4 \pm 1.0$  per meg, double the value at the surface and more repre-

---

L. Resplandy  
Scripps Institution of Oceanography, University of California San Diego, USA  
Tel.: +858-534-9944  
E-mail: lresplandy@ucsd.edu. R. F. Keeling  
Scripps Institution of Oceanography, University of California San Diego, USA.  
B. B. Stephens  
National Center for Atmospheric Research, Boulder, Colorado, USA.  
J. D. Bent  
National Center for Atmospheric Research, Boulder, Colorado, USA.  
A Jacobson  
Earth System Research Laboratory, NOAA, Boulder, Colorado, USA.  
C. Rödenbeck  
Max Planck Institute for Biogeochemistry, Jena, Germany.  
S. Khatiwala  
Lamont-Doherty Earth Observatory of Columbia University, Palisades, New York, USA.

sentative of large-scale air-sea fluxes. The global northward ocean heat transport asymmetry necessary to explain the observed APO deficit is about 0.6-1 PW, which corresponds to the upper range of estimates from hydrographic sections and atmospheric reanalyses.

**Keywords** Ocean heat transport · Potential oxygen · Hemispheric asymmetry · HIPPO aircraft campaign

## 1 Introduction

Major advances in our understanding of the large scale ocean can be related to the World Ocean Circulation Experiment (WOCE), which was a multinational ship-based program of unprecedented scale in the 1990s to measure ocean circulation and related transports of heat, salt, carbon, and nutrients. Though great strides were made on many fronts, WOCE did not provide a complete picture of the air-sea fluxes and large scale ocean transports. These needs are still unfilled to this day, despite the advent of the Argo float program and other improvements in sensor oceanography and satellites. The root difficulty is that many elements of the ocean circulation are still too uncertain to infer reliable fluxes and transports.

The ocean gains heat in the tropics and carries it poleward. The ocean heat transport is not symmetric about the equator, however, as the Atlantic overturning circulation transports heat from deep within the Southern Hemisphere to the Northern Hemisphere (Crowley 1992; Marshall et al 2014; Schneider et al 2014). This asymmetry in ocean heat transport is a key driver of the climate

mean state and variability through its influence on sea surface temperatures. Warmer sea surface temperature in the north are associated with larger oceanic heat loss to the atmosphere and a major factor causing the displacement of the inter-tropical convergence zone north of the equator (Philander et al 1996; Fuckar et al 2013; Marshall et al 2014; Schneider et al 2014). The northward meridional heat transport also controls climate variability on decadal to millennial timescales by regulating the sea ice cover in the Arctic and its positive feedback on natural and anthropogenic warming (Crowley 1992; Mahlstein and Knutti 2011). Northward heat transport is also invoked as a major driver of the variability associated with the North Atlantic Oscillation (Bryden et al 2014).

Estimates of the northward heat transport in the Atlantic range from 0.85 to 1.4 PW (1 Petawatt =  $10^{15}$  Watts) at approximately  $25^\circ\text{N}$  (Hall and Bryden 1982; Macdonald 1998; Bryden and Imawaki 2001; Ganachaud and Wunsch 2003; Talley 2003; Lumpkin and Speer 2007; Trenberth and Caron 2001; Trenberth and Fasullo 2008; Johns et al 2011). The Atlantic contribution is partly counterbalanced by southward transport in other basins resulting in a weaker net meridional transport for the whole ocean. The uncertainties, already significant in the Atlantic basin, increase dramatically when considering the net global transport. A useful measure of the ocean heat transport asymmetry ( $A_Q$ ) is:

$$A_Q = (T_{20^\circ N} + T_{20^\circ S})/2 \quad (1)$$

where  $T_{20^\circ N}$  and  $T_{20^\circ S}$  are the ocean meridional heat transports at  $20^\circ N$  and  $20^\circ S$  either estimated directly from hydrographic sections or computed from steady-state air-sea flux poleward of these latitudes. This metric is effectively an interpolated estimate of the transport across the Equator, but in contrast to estimates of the transport across the Equator is less sensitive to details of the tropical ocean circulation. Estimations from WOCE hydrographic sections (Ganachaud and Wunsch 2003) give a heat transport asymmetry between hemispheres of  $0.5 \pm 0.6$  PW, while indirect methods based on satellite observations and air-sea flux bulk formulations (Large and Yeager 2009) or radiative budgets at the top of the atmosphere (Trenberth and Caron 2001; Fasullo and Trenberth 2008) are spread between 0.1 and 0.8 PW. The long-term global ocean heat warming is of the order of 0.2 PW (Rhein et al 2013, or 274 ZJ over 40 years). Differences of the order of 0.5 PW between estimates of the heat transport asymmetry are a serious limitation to the understanding of the climate system and its variability.

The relatively weak observational constraint on the global ocean heat transport is matched by similarly large differences between global climate models. Hemispheric ocean heat transport asymmetry ( $A_Q$ ) in climate models participating in the most recent assessment of the Intergovernmental Panel on Climate Change (IPCC) shows a large spread ranging from slight southward or null transport to intense northward transport larger than 1 PW (see Figure 9.21 in Flato et al 2013). Inaccuracy and uncertainties of the order of 0.5-1 PW in the simulated ocean heat transport limits future climate predictions,

such as the prediction of El Niño Southern Oscillation and its teleconnections, or shifts in the ITCZ and rainfall associated with climate change (Ham and Kug 2012; Li and Xie 2014).

Here, we show that an additional constraint on the magnitude of the ocean heat transport asymmetry is provided by observations of atmospheric  $O_2$  and  $CO_2$  combined into a tracer called potential oxygen ( $PO = O_2^* + 1.1 \times CO_2$ ).  $PO$  was first defined in the atmosphere as atmospheric potential oxygen, a weighted sum of  $O_2$  and  $CO_2$  concentrations, to isolate the oceanic contribution from the land contribution in atmospheric variations of  $CO_2$  and  $O_2$  (Stephens et al 1998).  $APO$  is nearly unchanged by photosynthesis and respiration of land plants because of compensating influences on  $O_2$  and  $CO_2$ , which are exchanged in a  $-O_2:CO_2$  ratio of  $\sim 1.1$  (Severinghaus 1995). The primary influences on  $APO$  are air-sea exchange of  $O_2$  and  $CO_2$ , which are not tightly coupled to each other, and fossil-fuel burning, which have  $-O_2:CO_2$  ratios higher than 1.1, depending on the fuel type. Because the fossil-fuel influences are relatively well known,  $APO$  measurements can be used to constrain the weighted sum of  $O_2$  and  $CO_2$  fluxes across the air-sea interface.

$O_2$  and  $CO_2$  air-sea fluxes are driven by changes in solubility, ocean biology and physics. The solubility pump has a similar impact on both gases: when the ocean warms, it releases  $O_2$  and  $CO_2$  to the atmosphere and when it cools it uptakes both. In contrast, the biological pump has opposed effects on  $O_2$  and  $CO_2$ . Marine photosynthesis consumes carbon and produces  $O_2$  in surface waters, whereas the respiration of sinking organic matter depletes  $O_2$  and

adds carbon to deeper waters. The ocean circulation transports and mixes the gradients set by biological activity, favoring the uptake of  $O_2$  and the release of  $CO_2$  where deep waters re-surface (e.g. winter mixing and upwelling). While sources and sinks of  $O_2$  and  $CO_2$  are closely coupled within the ocean by the stoichiometry of marine photosynthesis and respiration, the fluxes across the air-sea interface driven by these processes are not so closely coupled, owing to differences in the  $CO_2$  and  $O_2$  equilibration times. As for land biospheric fluxes, however, the marine biologically-driven air-sea exchanges of  $O_2$  and  $CO_2$  do partly cancel. As a result, the thermally driven contributions of  $O_2$  and  $CO_2$  fluxes tend to dominate in terms of their impact on APO. A close link between APO and heat fluxes is expected because the thermally-induced gas fluxes of  $O_2$  and  $CO_2$  are closely tied to the net air-sea heat flux.

A close link between PO and heat exchange is also expected based on the hydrographic distribution of  $O_2^*$  and  $C^*$ , which are quasi-conservative ocean tracers that track air-sea exchange of  $O_2$  and  $CO_2$  (Gruber et al 2001; Gruber and Sarmiento 2002). As shown in Figure 1, the global ocean distribution of oceanic potential oxygen ( $OPO = O_2^* + 1.1 \times C^*$ ) is very strongly correlated with potential temperature (slope of  $-15.6 \mu\text{mol Kg}^{-1} \text{K}^{-1}$ ,  $r^2=0.95$ ). The gain of OPO by a parcel of water at the air-sea interface has to be associated with a loss of heat. We expect this relationship to also apply to the interhemispheric transport, such that the northward transport of heat should be associated with an uptake of  $O_2$  and  $CO_2$  in the northern hemisphere and release in the southern hemisphere. A deficit in APO, which mirrors the stronger uptake of

O<sub>2</sub> and CO<sub>2</sub> has indeed been observed in the Northern Hemisphere (Stephens et al 1998; Battle et al 2006; Keeling and Manning 2014) but this observation has not been previously used as a constraint of ocean heat transport.

Here, we present a framework based on oceanic and atmospheric chemical data that is sensitive to the ocean circulation patterns, and can thus be used to challenge models of ocean circulation and their predictions in terms of heat transport. Building up on previous work (Gruber et al 2001; Jacobson et al 2007; Mikaloff Fletcher et al 2007), we use a consistent application of inverse techniques to estimate air-sea fluxes of O<sub>2</sub>, CO<sub>2</sub> and heat. We simulate the APO distribution resulting from the inverse air-sea fluxes using an atmospheric transport model and additional fluxes from fossil-fuel burning, seasonal air-sea exchanges, and oceanic uptake of anthropogenic CO<sub>2</sub>. To explore the sensitivity of the northern APO deficit to the ocean transport, we used seven different ocean models that differ significantly in their large-scale circulation and transport. Simulated APO deficit in the Northern Hemisphere are then evaluated against recent observations from the High-Performance Instrumented Airborne Platform for Environmental Research (HIAPER) Pole-to-Pole Observations (HIPPO) large-scale aircraft campaign (Wofsy and the HIPPO Science Team and Cooperating Modellers and Satellite Teams 2011) and from the 20-year long surface sampling performed by the Scripps Institution of Oceanography (e.g. Keeling and Manning 2014). The comparison of the two independent atmospheric datasets with model results reveals that a north-

ward heat transport in the upper range of previous estimations is necessary to explain the observed APO deficit.

## 2 Methods

### 2.1 Atmospheric observations

This study takes advantage of two complementary APO datasets: one from the airborne HIPPO campaign (Wofsy and the HIPPO Science Team and Cooperating Modellers and Satellite Teams 2011) and the other from the nine-station surface flask network from the Scripps Institution of Oceanography (Keeling et al 1998; Stephens et al 1998; Keeling and Manning 2014). Both APO datasets rely on a combination of flask and *in situ* CO<sub>2</sub> concentrations and O<sub>2</sub>/N<sub>2</sub> ratios sampled along a similar meridional transect in the Pacific (Figure 2). The HIPPO data resolve the vertical distribution of APO over the troposphere based on 7 mid-Pacific transects covering the seasonal cycle between 2009 and 2011. The surface stations cover a 20-year period with bi-monthly sampling.

APO (in per meg) is calculated from measurements of CO<sub>2</sub> concentrations and O<sub>2</sub>/N<sub>2</sub> ratios (Stephens et al 1998) according to:

$$APO \text{ [per meg]} = \delta(O_2/N_2) + \frac{1.1}{X_{O_2}} * (CO_2 - 350 \text{ [ppm]}) \quad (2)$$

with

$$\delta(O_2/N_2) \text{ [per meg]} = \left[ \frac{(O_2/N_2)_{sample}}{(O_2/N_2)_{reference}} - 1 \right] * 10^6 \quad (3)$$



where  $\delta(O_2/N_2)$  is in per meg,  $CO_2$  in ppm, 1.1 is the approximate ratio of  $O_2$  production to  $CO_2$  consumption in terrestrial carbon storage (Severinghaus 1995),  $X_{O_2}$  is the atmospheric mole fraction of  $O_2$  necessary to convert  $[CO_2]$  from ppm to per meg units ( $X_{O_2} = 0.2095$ ), and 350 is an arbitrary reference for  $CO_2$ .

Here we focus on the northern APO deficit, which we quantify in three different ways: 1) the weighted difference between northern and southern hemisphere APO surface stations following (Hamme and Keeling 2008) (noted  $\Delta APO$  surface), where the weighting takes into account the distribution of the stations with latitude following Hamme and Keeling (2008); 2) the difference between the meridionally integrated APO content north of  $20^\circ N$  ( $20^\circ N$ - $80^\circ N$ ) and south of  $20^\circ S$  ( $58^\circ S$ - $20^\circ S$ ) from 900 mb HIPPO data (noted  $\Delta APO$  900mb) and 3) the same as 2) but column-averaged over the troposphere up to 400 mb (noted  $\Delta APO$  column). Further details on APO sampling, uncertainties and spatio-temporal interpolation used to derive annual mean values are presented in Appendix A.

## 2.2 Ocean observations

We use ocean interior data from the GLobal Ocean Data Analysis Project (GLODAP) version 1 (Key et al 2004). Conservative tracers related to air-sea fluxes  $C^*$  and  $O_2^*$  are computed following (Gruber et al 2001; Gruber and

Sarmiento 2002).

$$\begin{aligned} C^* &= DIC - \Delta DIC_{Bio} \\ &= DIC - R_{C:P}PO_4 - 1/2(Alk + R_{N:P}PO_4) \end{aligned} \quad (4)$$

$$\begin{aligned} O_2^* &= O_2 - \Delta O_{2Bio} \\ &= O_2 - R_{O:P}PO_4 \end{aligned} \quad (5)$$

All concentrations including DIC, phosphate ( $PO_4$ ) and alkalinity (Alk) are salinity normalized to account for dilution changes.  $R_{N:P}=170$ ,  $R_{C:P}=16$  and  $R_{O:P}=-170$  are the elemental ratios we use to ensure the conservation of  $C^*$  and  $O_2^*$  with respect to marine photosynthesis (Anderson and Sarmiento 1994). We compute the pre-industrial component of  $C^*$  used in our ocean inversion as follows:

$$C_{pi}^* = C^* - C_{anth} \quad (6)$$

where  $C_{anth}$  is the anthropogenic component of dissolved inorganic carbon from Khatiwala et al (2009). This subtraction is done at each observational point. Pre-industrial oceanic potential oxygen ( $OPO_{pi}$ ) is then computed as:

$$OPO_{pi} = O_2^* + 1.1 \times C_{pi}^* \quad (7)$$

Dissolved  $N_2$  concentrations are computed following Hamme and Emerson (2004) using GLODAP temperature and salinity (see details in Appendix B).

### 2.3 Ocean interior inversion and potential oxygen air-sea flux

We compute global distributions of air-sea fluxes using the ocean inversion technique of Gloor et al (2001); Gruber et al (2001) and Mikaloff Fletcher et al (2007), which yields steady-state fluxes based on ocean interior data and modeled ocean transport. The choice of the inversion technique is motivated by its ability to get observation-based estimates of all air-sea fluxes ( $\text{CO}_{2pi}$ ,  $\text{O}_2$ ,  $\text{N}_2$  and heat) in a consistent framework. Our application of the inverse method is limited to deriving steady-state pre-industrial fluxes. We assume that  $\text{O}_2$ ,  $\text{N}_2$  and heat contemporary fluxes are similar to the pre-industrial fluxes and therefore can be computed directly from  $\text{O}_2^*$ ,  $\text{N}_2$  solubility and potential temperature respectively. For example, changes in atmospheric  $\text{O}_2$  concentration due to anthropogenic activities (fossil fuel burning and land use) are estimated to be less than 0.1% (Keeling and Manning 2014), while changes in oceanic  $\text{O}_2$  concentrations due to climate change are of the order of  $\sim 40 \text{ Tmol y}^{-1}$  (Keeling et al 2010), which represents less than 0.1% of the  $\text{O}_2$  content in surface waters ( $< 100 \text{ m}$ ). The inverse calculation for  $\text{CO}_2$  is done exclusively on the  $C_{pi}^*$  component, thus deriving an estimate of the pre-industrial air-sea  $\text{CO}_2$  flux. Further details on the ocean inversion and its uncertainties are presented in Appendix B.

## 2.4 Ocean transport models

We carry out the ocean inversion calculation using ocean transports from seven different ocean models that differ significantly in their large scale circulation. Five of the ocean models used in the inversion are from the MOM suite (Jacobson et al 2007) and two are MITgcm models (Marshall et al 1997). The MOM suite (Table 1) was designed to explore the impact of a wide range of transports that reproduced the observed density distribution in the ocean (e.g. Gnanadesikan et al 2002; Palter et al 2010). It includes MOM-HH (high diapycnal and eddy diffusivity), MOM-LHS (low diapycnal diffusivity and high eddy diffusivity in Southern Ocean), MOM-LL (low diapycnal and eddy diffusivity), MOM-PSS (sometimes referred as P2A, low diapycnal diffusivity, high eddy diffusivity in Southern Ocean, narrow Drake Passage) and MOM-RDS (sometimes referred as P2, low diapycnal diffusivity, high eddy diffusivity in Southern Ocean, salinity restoring), all on a coarse resolution grid of  $4^\circ \times 5^\circ$ . The 2 MITgcm models provide further insight on the sensitivity to ocean transport, with the coarse resolution model ( $2.8^\circ$ , denoted MITgcm-2.8) and the  $1^\circ \times 1^\circ$  ocean state estimate ECCO1 (denoted MITgcm-ECCO) that assimilates numerous satellite and in-situ observations (Wunsch et al 2009).

To quantify the differences in large-scale ocean circulation between the seven models, we used the scheme of Gnanadesikan (1999), which divides the deep meridional overturning circulation (MOC) into three components: 1) dense water formation and sinking in the North Atlantic ( $M_{North}$ ), 2) upwelling of deep waters in the thermocline due to the downward mixing of

heat transforming dense waters into lighter waters ( $M_{Upwelling}$ ) and 3) the net conversion of deep to thermocline water in the Southern Ocean ( $M_{South}$ ), reflecting the balance between Ekman and eddy components (Figure 3 and Table 1).

All the OGCMs used here have rates of dense water formation in the North Atlantic of about 15-20 Sv, in agreement with observation-based estimates (Talley 2008; Lumpkin and Speer 2007). Their circulations differ mainly by the relative contribution of the tropical upwelling and the wind-driven transport in the Southern Ocean in returning deep waters to the surface (Table 1). MOM-HH, MOM-RDS and MITgcm-2.8 are dominated by the deep tropical upwelling ( $>13$  Sv). In the extreme case of MOM-HH, the tropical upwelling even surpasses the North Atlantic deep water formation ( $\sim 24$  Sv) and leads to a southward flow in the Southern Ocean ( $M_{South} = -8.4$  Sv). In contrast, MOM-PSS and MITgcm-ECCO are characterized by strong northward wind-driven flow in the Southern Ocean ( $\sim 12$  Sv) and weak tropical upwelling ( $< 8$  Sv). Finally, MOM-LL and MOM-LHS lie somewhere in between, with a relatively strong contribution of the tropical upwelling ( $\sim 11$  Sv) and a significant wind-driven flow from the south ( $\sim 4$  Sv). Refer to Appendix B for a description of the ocean models and how this study differs from previous studies.

## 2.5 Atmospheric transport modelling

We used the 3-D Eulerian atmospheric transport model (ATM) Tracer Model version 3 (TM3, Heimann and Körner 2003) to simulate annual mean APO

distributions using inverse  $O_2$  and  $CO_{2pi}$  air-sea fluxes combined with several different components: 1)  $N_2$  fluxes also from the same inversions; 2) Air-sea fluxes of anthropogenic  $CO_2$  from Khatiwala et al (2009), 3) uptake of  $O_2$  and  $CO_2$  from fossil fuel burning from the Emission Database for Global Atmospheric Research (EDGAR, available at <http://edgar.jrc.ec.europa.eu>); and 4) seasonal  $O_2$ ,  $CO_2$  and  $N_2$  components from Garcia and Keeling (2001), Rödenbeck et al (2013) and based on solubility changes expected from the seasonality in heat fluxes Keeling and Shertz (1992) respectively.  $N_2$  fluxes are relevant to derive APO as they modify the  $O_2/N_2$  ratio measured in the atmosphere (Equation 2). The seasonal components are relevant because of the so-called rectifier effect, in which interactions between seasonal variations in atmospheric transport and seasonal surface fluxes influence the annual mean. Further details on APO simulation and uncertainties from the different source components can be found in Appendix C.

The TM3 model carries excesses or deficits in  $O_2$ ,  $N_2$  and  $CO_2$  as if all three were trace gases in  $\mu\text{mol mol}^{-1}$  (ppm) units. To allow comparison to observations, changes in APO in per meg units are computed following Stephens et al (1998):

$$\begin{aligned}\Delta APO &= \frac{\partial APO}{\partial O_2} \times \Delta O_2 + \frac{\partial APO}{\partial N_2} \times \Delta N_2 + \frac{\partial APO}{\partial CO_2} \times \Delta CO_2 \\ &= \frac{1}{X_{O_2}} \times \Delta O_2 - \frac{1}{X_{N_2}} \times \Delta N_2 + \frac{1.1}{X_{O_2}} \times \Delta CO_2\end{aligned}\quad (8)$$

where  $\Delta O_2$ ,  $\Delta N_2$  and  $\Delta CO_2$  are the changes in ppm and  $X_{O_2}$  and  $X_{N_2}$  the atmospheric mole fractions of  $O_2$  and  $N_2$  ( $X_{O_2}=0.2095$  and  $X_{N_2}=0.7808$  ).

TM3 was run at a horizontal resolution of  $4^\circ$  latitude by  $5^\circ$  longitude with 19 vertical levels and driven by 6-hourly meteorological fields derived from reanalyses between 1990 and 2013. To explore sensitivity to atmospheric circulation, winds from two reanalyses were used: NCEP (Kalnay et al 1996) and ERA-Interim (Dee et al 2011). Annual mean values of  $\Delta\text{O}_2$ ,  $\Delta\text{N}_2$ , and  $\Delta\text{CO}_2$  were computed from the last 10 years (1994-2013). Monthly mean ATM outputs were sampled at the station locations to allow direct comparison with surface Scripps data. The northern APO deficit was computed following the same approach as in observations (see section 2.1).

### 3 Results

#### 3.1 General features of diagnosed air-sea fluxes

##### 3.1.1 $\text{O}_2$ , $\text{N}_2$ and pre-industrial $\text{CO}_2$ fluxes

The  $\text{O}_2$ ,  $\text{N}_2$  and  $\text{CO}_{2pi}$  air-sea fluxes obtained from the inverse calculations are in qualitative agreement with the previous results of Gruber et al (2001), Mikaloff Fletcher et al (2007) and Gerber and Joos (2010) (Figure 4). The tropical band is the major outgassing region of  $\text{CO}_{2pi}$ ,  $\text{O}_2$  and  $\text{N}_2$ . The ocean at mid-latitude and high latitude in the northern hemisphere is on average a sink for the 3 gases. In contrast,  $\text{CO}_{2pi}$  fluxes in the southern hemisphere are generally opposed to  $\text{O}_2$  and  $\text{N}_2$  fluxes, with the ocean being a large sink of  $\text{CO}_{2pi}$  and a source of  $\text{O}_2$  at mid-latitude and a source of  $\text{CO}_{2pi}$  and a sink of  $\text{O}_2$  and  $\text{N}_2$  at high latitude.

Two features that are quite sensitive to the ocean transports are the strength of the tropical outgassing and the balance between southern mid-latitudes and southern high-latitudes (Figure 4). For example in the tropical band, the outgassing of  $O_2$  is about 30% stronger in the inverse calculation with MOM-HH than with MITgcm-ECCO. At southern mid-latitudes, the outgassing of  $O_2$  varies by a factor larger than 10 between MOM-RDS and MOM-PSS. Another sensitive feature is the distribution of the northern hemisphere ingassing of  $O_2$  and  $N_2$  between mid-latitudes and high-latitudes. This mostly arises from the differences in the representation of the North Atlantic winter mixing, which is more concentrated north of  $49^\circ N$  in the MITgcm runs than in the MOM-suite runs.

$CO_{2pi}$  air-sea fluxes computed here are similar to the previously published runs (Mikaloff Fletcher et al 2007; Gerber and Joos 2010) but there are significant differences between  $O_2$  and  $N_2$  fluxes and those published in Gruber et al (2001). In particular, the ocean uptake in the northern hemisphere is mostly located at mid-latitude in Gruber et al (2001), while it is at higher latitude in our estimate (Figure 4). This difference is related to the lower resolution of the inversion used in Gruber et al (2001) (13 vs. 21 regions, Table 6).



### 3.1.2 Relation between heat and pre-industrial potential oxygen air-sea fluxes

The flux of pre-industrial potential oxygen across the air-sea interface is computed from the combination of  $O_2$  and  $CO_{2pi}$  inverse fluxes:

$$F_{PO_{pi}} = F_{O_{an}} + F_{C_{pi}} \quad (9)$$

where  $F_{O_{an}}$  and  $F_{C_{pi}}$  are the annual mean air-sea fluxes of oxygen and pre-industrial carbon obtained for each ocean inversion. We find that the  $PO_{pi}$  air-sea flux is strongly anti-correlated by zone to the air-sea heat flux (Figures 5 and 6). This relationship is insensitive to the ocean model with an ocean loss of about  $120 \text{ Tmol y}^{-1}$  of  $PO_{pi}$  for a heat uptake of 1 PW and *vice versa*, which is equivalent to a slope of  $-3.8 \text{ nmol J}^{-1}$  similar to the strong correlation between  $OPO_{pi}$  and potential temperature noted earlier (slope of  $-3.9 \text{ nmol J}^{-1}$  on Figure 1).

The large-scale anti-correlation between heat and  $PO_{pi}$  fluxes is reflected in the opposed hemispheric asymmetry in heat and  $PO_{pi}$  ocean transport (defined as the average of the fluxes across  $20^\circ\text{N}$  and  $20^\circ\text{S}$ , see Equation 1, Figure 6). All models except MOM-HH show a net northward heat transport asymmetry, with a magnitude that is closely tied to the southward  $PO_{pi}$  flux (Figure 6).

### 3.2 Observational constraints on air-sea fluxes and oceanic transports

#### 3.2.1 Ocean meridional heat transport

Figure 7 compares the ocean heat transports derived from the inverse calculations against estimates based on hydrographic sections by Macdonald (1998), Ganachaud and Wunsch (2003), Talley (2003) and Johns et al (2011). In the Atlantic, our inverse estimates are generally weaker, in particular at low latitude where they underestimate the transport by  $\sim 0.2\text{--}0.6$  PW (Figure 7b). In the North Pacific, estimates from two hydrographic sections suggest that inverse results underestimate the northward transport between  $35^\circ\text{N}$  and  $50^\circ\text{N}$ , the latitudes of the Kuroshio Current (Figure 7c). As a result, the northward transport in the Northern Hemisphere at global scale is underestimated by at least 0.2 PW and possibly by as much as 1 PW (Figure 7a).

In the Southern Hemisphere, the large spread in the southward heat transport at  $10^\circ\text{S}$ – $50^\circ\text{S}$  ( $-2$  PW to  $-1$  PW) is dominated by the Indo-Pacific (Figure 7a, c). Transports from hydrographic sections are in the weaker end or lower than the transports obtained from the inverse computation and exclude the estimate of MOM-HH, which is characterized by strong southward heat transport and a southward return flow in the Southern Hemisphere (Table 1). However, only three sections associated with large uncertainties are available in the southern Indo-Pacific, which prevents us from constraining further the heat transport at the global scale.

### 3.2.2 Observed APO distribution with latitude

As shown in Figure 2a, annual mean surface APO is maximum in the tropics with values relative to Cape Grim of  $1.2 \pm 1$  per meg at the American Samoa Observatory and decreases towards higher latitudes, reaching  $-6 \pm 1.2$  per meg at Palmer station in the southern hemisphere and  $-9.5 \pm 2.2$  per meg at Alert station in the northern hemisphere. Observations along the HIPPO transect confirm the presence of an APO deficit of 5-20 per meg in the northern hemisphere, first noted by Stephens et al (1998) and an APO excess of 5-10 per meg near the equator in the Southern hemisphere, referred to the equatorial bulge in previous studies (Figure 2b, Stephens et al 1998; Battle et al 2006; Tohjima et al 2005, 2012).

### 3.3 Components of modeled APO gradients

We computed APO gradients from inverse annual mean  $O_2$ ,  $CO_{2pi}$  and  $N_2$  fluxes, combined with the additional components due to the seasonal rectifier effect for all three gases, the anthropogenic carbon air-sea flux and fossil fuel burning. Figure 8 shows the total APO gradient and its components at the surface and averaged over the atmospheric column. The wind product (NCEP vs ERA-Interim) has only a weak impact on the latitudinal gradient obtained on those large spatial and temporal scales (Figure 8a). Fossil fuel burning and anthropogenic carbon components oppose each other and together produce only a small contribution to the north-south gradient at the surface and in

average over the column (Figure 8b, c). Note that the contributions of fossil fuel and anthropogenic carbon are relatively well known and therefore introduce little uncertainty in the modeled APO gradient (Table 2).

The seasonal rectifier effect mostly increases annual mean surface APO values at mid- and high-latitudes and produces a deficit at low latitudes (Figure 8b), because vertical mixing over the ocean is weak in summer when  $O_2$  is outgassing and strong in winter when  $O_2$  is ingassing. According to the atmospheric transport model used here (TM3), the excess due to the rectifier effect at the surface is larger in the north than in the south, so that the rectifier contributes to reduce the surface northern deficit arising from the other components. This effect has been shown to be sensitive to the transport model used (Stephens et al 1998; Blaine 2005; Battle et al 2006). Column averaged data and model are, however, less sensitive to the rectifier (Figure 8c), due to compensation of high rectifier values at the surface, where summer trapping of APO occurs, and lower values aloft (Figure 9). As a result, the uncertainty related to the rectifier effect is relatively small when considering column-averaged APO values (Table 2). In addition to lower rectifier uncertainties, column-averaged values are more representative of annual large-scale air-sea fluxes as they integrate local air-sea fluxes, mostly captured at the surface, and remote air-sea fluxes, captured aloft after being mixed vertically and transported horizontally in the troposphere (Figure 2b,c and Figure 8).

### 3.4 Model/data comparison of northern APO deficit

Model APO gradients at surface stations are compared to observations (Figure 2a). Of all estimates, the inversion using MITgcm-ECCO is best at reproducing the 10 per meg deficit in APO between Alert and Cape Grim. The worst performing inversion is MOM-HH, which predicts a reverse gradient with excess APO in the north, consistent with the deficiency noted above in MOM-HH for the heat transport.

The three different metrics of the northern APO deficit (surface, 900 mb, and column averaged) are compared against each other and against the heat transport asymmetry in Figure 10. At the surface the observed APO northern deficit is  $-4.9 \pm 0.9$  per meg from surface stations and  $-5.7 \pm 1.5$  per meg from airborne data at 900 mb (Figure 10a, see method detail in section 2.1). The agreement between those two metrics, which are derived from different spatiotemporal coverage and different sampling techniques, shows that this gradient is quite well resolved. The column-averaged deficit is about 4 per meg stronger than the gradient at 900 mb ( $-10.4 \pm 0.9$  per meg, Figure 10b). The column gradient is strengthened by the notably low APO values observed in the mid-troposphere between  $40^\circ\text{N}$  and  $60^\circ\text{N}$  (Figure 2b). Seasonal HIPPO transects (B. Stephens, pers. Comm.) show that this mid-tropospheric deficit in APO is strongly influenced by a deficit in  $\delta(\text{O}_2/\text{N}_2)$  in the northern hemisphere during winter.

Simulations using MITgcm-ECCO, MOM-PSS, MOM-LHS and MOM-LL succeed at reproducing the northern APO deficit at the surface within the error

bars (Figure 10a). Simulations based on other ocean models mostly represent smaller northern APO deficits. In contrast, all models fail at capturing the vertically integrated northern APO deficit (Figure 10b and Table 2). This is explained by the clear underestimation of the mid-tropospheric APO minimum in the north as can be seen by comparing Figure 2b and 2c). The extent of this underestimation varies, with MITgcm-ECCO, MOM-PSS, MOM-LHS and MOM-LL reproducing about 65% ( $-5.9$  to  $-6.4 \pm 0.8$  per meg), MOM-RDS and MITgcm-2.8 about 50% ( $-5.0$  to  $-5.2 \pm 0.8$  per meg) and MOM-HH only 40% ( $-3.9 \pm 0.8$  per meg) of the observed northern deficit.

Figure 10c shows that the magnitude of the northern APO deficit is strongly correlated with the heat transport asymmetry across models, with stronger northern deficits, associated with stronger northern heat transport. If we extrapolate based on this correlation, the underestimation of the APO deficit by  $\sim 3$  per meg in MITgcm-ECCO corresponds to an underestimation of the northward ocean heat transport of  $\sim 0.5$ - $0.6$  PW globally (Figure 10c). The global meridional heat transport needed to explain the observed APO deficit is  $0.6$ - $1$  PW, which is in the upper range of the Ganachaud and Wunsch (2003) estimate based on hydrographic sections and in agreement with the estimate of Large and Yeager (2009) based on air-sea fluxes bulk formulations (Figure 10c).

### 3.5 Model/data comparison of APO gradient in the Southern Hemisphere

Figure 11 shows the Samoa-to-Cape Grim APO latitudinal gradient at the surface and how it relates to the meridional heat transport at  $20^{\circ}\text{S}$ . Surface observations show a slight excess in APO at Samoa compared to Cape Grim of  $1.6 \pm 0.6$  per meg. In comparison, the inverse models yield an APO excess at Samoa compared to Cape Grim that is systematically too large, probably due to the underestimation of the PO ingassing in the Southern Ocean and/or the overestimation of the PO outgassing in the tropics. MITgcm-ECCO reproduces best the Samoa-to-Cape Grim difference ( $\sim 2.8$  per meg) followed by MOM-LHS, MOM-LL and MOM-PSS ( $\sim 3.5$  per meg), while MOM-RDS, MITgcm-2.8 and MOM-HH predict unrealistic gradients, two to four times larger than the observations (Figure 11).

The APO gradient between Samoa and Cape Grim computed by the inverse models is closely related to the heat transport at  $20^{\circ}\text{S}$ . Weaker APO gradients are associated with weaker southward heat transports (Figure 11). The overestimation of the Samoa APO excess therefore implies an overestimation of the southward heat transport across  $20^{\circ}\text{S}$ . Uncertainties on this constraint are relatively large. The observed APO gradient between Samoa and Cape Grim has a weak signal-to-noise ratio, the estimation of a robust annual mean from the 15-year time-series being influenced by interannual variability (0.6 per meg compared to a gradient of 1.6 per meg). In addition, the APO gradient sums the contribution of annual mean steady-state, which is related to the heat transport ( $\sim 2.90$  per meg), with other contributions of the same order of

magnitude: the rectifier effect ( $-2.80 \pm 0.60$  per meg), the signature of fossil fuel ( $-1.10 \pm 0.05$  per meg) and the effect of anthropogenic carbon uptake ( $2.60 \pm 0.50$  per meg). However, the 20-year long time-series available at surface stations allow to estimate the weak annual APO gradient with some confidence, which would be more difficult with the observations along the HIPPO transects. The APO-to-heat relationship derived from our inverse estimates and the observed APO gradient point towards a southward meridional heat transport at  $20^\circ\text{S}$  of 0.2 to 0.8 PW, in the lower range of hydrographic section estimates ( $0.8 \pm 0.6$ ) and in agreement with air-sea bulk formulations (Figure 11).

## 4 Discussion

### 4.1 Northern APO deficit supports strong ocean heat transport asymmetry

The hemispheric asymmetry in APO observed in the atmosphere demands a larger oceanic uptake of potential oxygen ( $\text{PO} = \text{O}_2 + 1.1 \times \text{CO}_2$ ) in the northern hemisphere and a southward transport of OPO in the ocean to maintain the asymmetry. We used inverse methods based on ocean observations and seven models of ocean circulation to compute air-sea fluxes of  $\text{O}_2$ ,  $\text{CO}_2$ ,  $\text{N}_2$  and heat and their predictions in terms of heat transport. We showed that PO and heat are tightly coupled via air-sea fluxes and ocean transport (slope of  $3.8 \pm 2 \text{ nmol J}^{-1}$ ). Using an atmospheric transport model, we obtained the atmospheric APO distribution expected from the seven air-sea fluxes simulations. Four of them, namely those using MITgcm-ECCO, MOM-PSS, MOM-LHS



and MOM-LL oceanic transports, reproduce the north-south APO gradient observed at the surface within the error bars ( $-5.5 \pm 1.5$  per meg).

The comparison at the surface is hampered, however, by uncertainties on the impact of seasonal fluxes on the annual mean, via the so-called rectifier effect (Stephens et al 1998; Battle et al 2006; Gruber et al 2001). A major achievement of this study relies on the extensive sampling effort deployed during the 2009-2011 HIPPO aircraft campaign. This dataset shows that the northern APO deficit in the mid-troposphere is almost two times larger than the one at the surface ( $-10.4 \pm 0.9$  per meg). These new observations reveal that although some of the estimates reproduce the northern APO deficit at the surface, they fail to reproduce the column-averaged gradient (Figure 10). The column-averaged annual gradient integrates the signal of local air-sea fluxes trapped in the seasonally-varying boundary layer as well as remote air-sea fluxes mixed by dominant meridional winds, and is therefore more representative of the large-scale global air-sea fluxes. Among the ocean transport schemes, MITgcm-ECCO yields a northern deficit with the best agreement with the observations, which could be expected as the MITgcm-ECCO model is a state of the art ocean state estimate that represents the circulation at higher resolution and assimilates satellite and in-situ data. Nevertheless the improvement of using MITgcm-ECCO is relatively small compared to three of the MOM inversions (MOM-PSS, MOM-LHS and MOM-LL) that predict very similar large-scale patterns and APO deficit, although they are based on ocean models at much lower resolution.

Failure to capture the column averaged northern APO deficit suggests that inverse solutions mis-represent the north-south asymmetries in annual mean potential oxygen (PO) fluxes. In reality, there is more PO uptake in the northern hemisphere and more release in the south than found in any of the inverse calculations. By this logic, the agreement with some of the models at the surface stations (Figure 10a) must partly be spurious, as a result of compensating errors in the surface fluxes and in atmospheric transport, possibly related to the rectifier effect. This is possible if the rectifier, particularly in the Northern Hemisphere, is underestimated in our study. In summer, the ocean poleward of  $40^\circ$  in both hemispheres is a source of PO and the atmospheric planetary boundary layer is shallow (Stephens et al 1998; Nevison et al 2008). The rectifier effect creates an annual mean APO excess near the surface at mid- and high-latitudes. We find that this excess is however larger in the north than in the south, probably because of continental masses reinforcing seasonal mixing differences in the north. A too weak rectifier effect would therefore artificially strengthen the surface northern deficit and explain the spurious agreement at the surface. The HIPPO data effectively back this point, by showing a considerably larger gradient in the mid troposphere than at the surface. This highlights the added value of airborne observations sampling the troposphere over surface-only measurements.

Although all simulations, regardless of ocean circulation model, systematically underestimate the northern APO deficit, they show a robust relationship between the deficit and the ocean heat transport asymmetry. Based on this

relationship, the hemispheric ocean heat transport asymmetry necessary to explain the observed northern APO deficit is about 0.6-1 PW. This estimate is in agreement with the most recent estimate based on air-sea flux bulk formulations (Large and Yeager 2009), falls in the upper range of transports derived from hydrographic sections (Ganachaud and Wunsch 2003) and is larger than top of the atmosphere budgets (Trenberth and Caron 2001; Fasullo and Trenberth 2008) (Table 3).

#### 4.2 Missing APO sink/heat source in Northern Hemisphere

HIPPO seasonal data suggest that the underestimation of the northern APO deficit in our inverse results is associated with a too weak oceanic uptake of oxygen during winter in the northern hemisphere. Two oceanic regions could trigger a strong winter APO decrease in the northern hemisphere: the North Atlantic and the western North Pacific. In both regions, winter deep/intermediate waters formation favors the ocean uptake of PO. In addition, those regions are characterized by extremely thick atmospheric planetary boundary layers in winter enabling the vertical mixing of low APO surface values up to 2000-2500 m altitude and the zonal transport by westerlies (Figure fs1 in supplementary material). It is relatively certain that the PO uptake is underestimated by the models in the North Atlantic. All inverse calculations underestimate the northward heat transport in the Atlantic by about 0.2-0.6 PW compared to hydrographic section estimates of Ganachaud and Wunsch (2003) and Talley (2003) (Table 3).

The failure to duplicate the APO deficit is most certainly tied to a similar deficit in the ability of these models to duplicate independent estimates of northward heat transport. This defect could have either of two causes, i.e. it could be caused by the oceanic transports being incorrect, or it could be due to a limitation of the inverse methodology, even for realistic transports. To address this issue, we also looked at the heat transports from the MITgcm-ECCO forward model. Interhemispheric heat transport asymmetry from the forward and inverse MITgcm-ECCO solution are the same in the Indo-pacific (-0.3 PW in Table 3) and similar in the Atlantic (0.5 and 0.6 PW in Table 3), which suggests that the inverse method is robust enough to capture large-scale meridional patterns. Despite a realistic overturning circulation ( $M_{North}=20$  Sv in Table 1) in agreement with observations (Talley 2008; Lumpkin and Speer 2007), the meridional heat transport in the MITgcm-ECCO forward model is in the lower range of observations in the northern hemisphere (1 PW at  $20^{\circ}$ N to be compared to observations in Figure 7a) and lower than most observations in the southern hemisphere (-0.3 PW at  $20^{\circ}$ S to be compared to observations in Figure 7a). However, it is difficult to investigate the details of the model biases. Where the data coverage is sufficient to capture the heat transport over a long time period, such as along the RAPID and Florida Straight surveys at  $26^{\circ}$ N (Johns et al 2008, 2011), MITgcm-ECCO falls in the range of observed interannual variability (Table 4). MITgcm-ECCO assimilates those data; the fact that it performs well where intense data coverage is available but underestimates the heat transport asymmetry at basin- and global-scale suggests

that observations are still too scarce in some regions to better constrain the ocean meridional heat transport in ocean state estimates.

The bias in the Atlantic meridional transport alone could explain most of the mismatch with APO observations. However, there is observational evidence that the sink of potential oxygen is also underestimated in the western North Pacific. Two hydrographic sections (Macdonald 1998; Talley 2003) suggest that the northward heat transport is also underestimated in the North Pacific where the Kuroshio Current is located (Figure 7c). In addition, Tohjima et al (2012) recently presented data showing a strong surface APO deficit in the western North Pacific associated with a gradient of 15 per meg between 20°S and 40°N. This gradient in the western Pacific is more than twice the gradient observed at the same latitude in the eastern/central Pacific (Figure 2a). This enhanced western Pacific uptake of PO, supports the existence of a stronger northward heat transport in the Pacific, absent from our inverse estimates but in agreement with some of the data-based estimates (Macdonald (1998) and Talley (2003) in Figure 7c).

#### 4.3 Insights on Southern Hemisphere heat transports

In addition to the possible model deficiencies in the Northern Hemisphere, large biases may also exist in the Southern Hemisphere. Meridional heat transports at 20°S are particularly ill-constrained and observational-based estimates range from -0.2 to -1.4 PW (Flato et al 2013). We consider the Samoa-to-Cape Grim APO difference as a proxy of the heat transport at 20°S. This metric

gives a measure of the northward transport of  $OPO_{pi}$  in the southern hemisphere and thereby provide some insight on the southward transport of heat at those latitudes. Inverse estimates overestimate the APO excess at Samoa compared to Cape Grim and the associated southward transport of heat at  $20^\circ\text{S}$ . Unlike the northern deficit that relies on a network of surface stations and airborne data, the Samoa-to-Cape Grim metric is based on the observations at 2 surface stations and is sensitive to the strength of the rectifier ( $2.8 \pm 0.6$  per meg). In addition, the noise-to-signal ratio of this metric is larger, which makes it more sensitive to possible systematic errors. The constraint on the heat transport at  $20^\circ\text{S}$  is therefore less robust than the constraint on the global meridional heat transport. Nevertheless, we evaluate the southward heat transport at  $20^\circ\text{S}$  to be -0.2 to -0.8 PW (southward), which is in agreement with the estimates of Large and Yeager (2009) and points towards the weakest end of hydrographic estimates (Ganachaud and Wunsch 2003). We find that inverse solutions best reproducing APO gradients in this region are based on models with stronger wind-driven upwelling in the Southern Ocean ( $M_{South}$ ) and weaker tropical upwelling ( $M_{Upwelling}$ , in table 1).

#### 4.4 Limitations and uncertainties

Having discussed the major insights of our study, we recognize that it is subject to certain limitations and that challenges await future studies. A major limitation of the current and previous studies based on ocean interior inversions is the assumption of steady state that gives no information on the transient

changes of biogeochemical and thermal air-sea fluxes, e.g. associated with natural or anthropogenic climate changes. The ocean heat content is increasing due to recent climate change at a rate of  $\sim 5 \text{ ZJ y}^{-1}$  (Rhein et al 2013) with the Southern Hemisphere taking up more heat due to larger ocean surface. Although there is no well-constrained estimate of the contribution of global warming on  $\text{CO}_2$  and  $\text{O}_2$  air-sea fluxes, we can estimate an upper bound of this effect as follows of this effect.

Assuming the extreme scenario where all  $5 \text{ ZJ y}^{-1}$  enter the ocean in the Southern Hemisphere, and assuming an APO to heat ratio of  $3.8 \text{ nmol J}^{-1}$ , we find that the ocean would release  $1.9 \times 10^{13}$  moles of APO in the Southern hemisphere (i.e.  $5 \times 10^{21} \times 3.8 \times 10^{-9}$ ). Assuming that the exchange time between the two hemispheres is one year, we find that the maximum impact of transient warming on the north-south APO gradient is  $\sim 1.0$  per meg (i.e.  $1.9 \times 10^{13} / 1.85 \times 10^{19} = 1.0 \times 10^{-6} = 1.0$  per meg, with  $1.85 \times 10^{19}$  being the number of moles of  $\text{O}_2$  in one hemisphere of the atmosphere). This back of the envelope estimation corresponds to a relatively small uncertainty of  $\sim 0.14 \text{ PW}$  on the northward heat transport.

The steady state hypothesis of the ocean inversion also prevents us from accounting for seasonal and interannual variability in ocean circulation and hydrographic data. The framework thereby neglects co-variations between time-varying fluctuations in concentration and velocity because both are assumed constant with time. However, there is observational evidence that the merid-

ional transport at depth varies from seasonal to interannual time scales (Johns et al 2011; Atkinson et al 2012).

Finally, another limitation of the method is the low spatial resolution used for both the ocean inversion and the ocean models used to compute ocean transports. The ocean inversions are performed over 30 oceanic regions, which prevents us from resolving air-sea flux spatial structures at smaller scale, such as the patchiness of  $O_2$  uptake and heat release during deep winter mixing. However, the relatively close agreement between the heat transport in the MITgcm-ECCO forward and inverse solutions (Table 3 and section 4.2) suggests this effect weakly influence the large-scale interhemispheric asymmetry.

The method can also not account for correlations on spatial scales smaller than the interior ocean model grid. Even the model with highest horizontal resolution (MITgcm-ECCO at  $1^\circ$  resolution) does not fully resolve the mesoscale field, which is likely to introduce errors in the ocean mean transport. Indeed, the ocean dynamics at small spatial scale influences the ocean circulation at larger scale including the shallow circulation associated with gyres, the deep meridional overturning circulation (Lévy et al 2010; Thomas and Zhai 2013; Mazloff et al 2013, e.g) and in turn lateral and vertical transports (Thomas and Ferrari 2008; Capet et al 2008; Resplandy et al 2011; Zhang et al 2014).

## 5 Conclusions

The major findings of this study are:



1. On the basis of a close correlation in hydrographic data, which is supported by inverse calculations, we find that the large-scale fluxes of potential oxygen ( $PO = O_2 + 1.1 \times CO_2$ ) are closely tied to heat fluxes.
2. HIPPO aircraft column-averaged data provide superior constraints on large-scale PO fluxes (compared to surface data) due to a lower sensitivity to rectifier effects and local air-sea fluxes.
3. Effects of fossil-fuel emissions and anthropogenic carbon uptake are significant, but largely cancel with relatively low uncertainty, allowing APO data to constrain pre-industrial  $O_2$  and  $CO_2$  fluxes.
4. APO data combined with the relationship found between PO and heat provide valuable constraints on: i) the interhemispheric asymmetry of the oceanic heat transport (northward transport between 0.6 and 1 PW) and ii) the southern meridional transport at  $20^\circ S$  (southern transport between 0.2 and 0.8 PW).
5. The constraints on heat transports obtained with APO converge with independent heat flux estimates from bulk formulations (Large and Yeager 2009) and are in the upper range of hydrographic estimates (Ganachaud and Wunsch 2003).
6. APO has the potential to be a more precise large-scale constraint, thus narrowing the uncertainty range of the heat transport asymmetry estimates based on hydrographic data.

## A Atmospheric observations: interpolation and uncertainties

### A.1 Scripps surface stations data

Observations at each station are fit with a four-harmonic seasonal cycle and a stiff long-term trend (Keeling and Manning 2014). Station annual means are computed from the de-trended seasonal fit and referenced to year 2009 in terms of fossil fuel burning and anthropogenic carbon uptake. Uncertainties on APO annual mean, northern deficit and Samoa to Cape Grim gradient arise from the interannual variability (the seasonal variability being resolved by the 15-year long record of observations). The uncertainty related to interannual variability  $\epsilon_{IA}$  was computed using a forward predictive model with an autoregressive process of order 2 (AR2). The predictive model was used to generate a 1500-year long time-series with the same mean and variance as the data. It quantifies the error made by estimating the mean from a temporally varying 15-year long time-series. It is computed as  $\pm$  the standard deviation between the 100 means (1500/15) estimated from 15-year long segments and the mean estimated from the 1500-year long time-series. Further details on Scripps APO measurements were presented in Keeling et al (1998), Stephens et al (1998), Hamme and Keeling (2008) and Keeling and Manning (2014).

### A.2 Aircraft data

The HIPPO campaign took place between January 2009 and September 2011 aboard the National Center for Atmospheric Research / National Science Foundations Gulfstream V research jet HIAPER and mapped the vertical and meridional distribution of atmospheric carbon cycle gases and other anthropogenic tracers including CO<sub>2</sub> and O<sub>2</sub>/N<sub>2</sub> (Wofsy and the HIPPO Science Team and Cooperating Modellers and Satellite Teams 2011). We used 7 of the 10 transects performed during the five HIPPO campaigns. These transects sample a similar Pacific section between 80°N and 58°S and cover the seasonal cycle one to two months apart (Figure 2 and Table 5). The data file we have used is that of Wofsy et al (2012) (*HIPPO\_all\_missions\_merge\_10s\_20121129.tbl*), but with an updated version of the

APO data. The APO data in the 20121129 file included an adjustment of the flask data for thermal fractionation that used the measured Ar/N<sub>2</sub> ratios. This adjustment also affected the in situ data which are adjusted to agree with the flasks. To avoid interhemispheric gradients in Ar/N<sub>2</sub> affecting our results, we have used a version of the APO data without this adjustment, and will include this version of the data in an upcoming update to the official HIPPO data repository. Three transects were removed because they sampled different longitudes. APO was computed similarly to surface stations based on CO<sub>2</sub> concentrations and O<sub>2</sub>/N<sub>2</sub> ratios at each data point (see equation 2). APO values were interpolated in space along this transect with a 5° longitude resolution and 19 vertical levels corresponding to the grid of the atmospheric transport model TM3 used in this study (see section C). We used a kriging interpolation method that computes the gaussian-weighted average based on the spatial covariance between triangulated data points, with a weighting radius spanning over 10° of latitude on the horizontal and 50 mb on the vertical.

We computed the northern APO deficit using data interpolated to ~900 mb (noted  $\Delta$ APO surface), which can be compared to the deficit derived from surface stations (section 2.1) and data vertically integrated over the troposphere between the surface and 400 mb (noted  $\Delta$ APO troposphere). The northern deficit was estimated using the 7 HIPPO transects and a bi-harmonic seasonal fit with periods of 1 year and 6 months after de-trending and referencing the data to year 2009 using the time-series at the Cape Grim surface station. Annual mean values of the surface and tropospheric deficit were computed from these seasonal fits.

The uncertainty on the annual mean includes the impact of spatio-temporal sparsity in the data. The uncertainty on  $\Delta$ APO related to interannual variability ( $\epsilon_{IA}$ ) is estimated similarly to the uncertainty on  $\Delta$ APO for surface stations using an auto-regressive process and taking into account that the mean is derived from a record spanning 3 years. At the surface,  $\epsilon_{IA} = \pm 1.2$  per meg. Integrated over the troposphere,  $\epsilon_{IA}$  is assumed to be 60% of the uncertainty at the surface. This estimate is based on the results of the atmospheric model TM3, in which the interannual variability of the northern deficit integrated vertically and meridionally is almost half of the one obtained at the surface. The uncertainty on  $\Delta$ APO

related to the spatio-temporal undersampling of the seasonal cycle  $\epsilon_{SEAS}$  is estimated by sub-sampling the APO distribution obtained with the atmospheric transport model TM3 at the time and place of HIPPO transects.  $\epsilon_{SEAS}$ , computed as  $\pm$  the difference between the "true" mean and the mean estimated by sub-sampling, is 0.4 per meg at the surface and 0.2 per meg when integrated over the troposphere.

## B Ocean interior inversions: computation of carbon, oxygen, nitrogen and heat air-sea fluxes

The atmospheric data are used to evaluate the fluxes of  $O_2$ ,  $CO_2$ ,  $N_2$  and heat from a suite of ocean inverse calculations, which we perform based on the method of Gloor et al (2001), Gruber et al (2001) and Mikaloff Fletcher et al (2007). These inverse calculations rely on ocean interior data from the GLObal Ocean Data Analysis Project (GLODAP) version 1 (Key et al 2004). Ocean interior heat was computed from GLODAP potential temperature and the sea water capacity of Millero et al (1973).  $N_2$  concentrations, not available in the database, were computed following Hamme and Emerson (2004) using temperature (T) and salinity (S):

$$\begin{aligned} \ln[N_2] &= A_0 + A_1 * Ts + A_2 * Ts^2 + A_3 * Ts^3 \\ &+ S * (B_0 + B_1 * Ts + B_2 * Ts^2) \\ Ts &= \ln\left(\frac{298.15 - T}{273.15 + T}\right) \end{aligned} \quad (10)$$

with  $A_0=6.42931$ ,  $A_1=2.92704$ ,  $A_2=4.32531$ ,  $A_3=4.69149$ ,  $B_0=-7.44129.10^{-3}$ ,  $B_1=-8.02566.10^{-3}$  and  $B_2=-1.46775.10^{-2}$ .

The inverse method relates interior tracer fields to air-sea fluxes using steady-state basis functions computed by releasing unit dye tracer at the surface of 30 oceanic regions in a ocean general circulation model (OGCM) (Mikaloff Fletcher et al 2006) (Figure 12). The basis function or footprint  $A_i$  obtained for region i essentially gives the contribution of the

air-sea flux of each surface region  $i$  to the concentration at each point in the ocean interior. The observed concentration is decomposed into contributions from each of the 30 regional sources:

$$C_{obs} = \sum_{i=1}^{30} \lambda_i A_i + \epsilon \quad (11)$$

with  $\lambda_i$  a dimensionless factor that scales the surface unit flux and  $\epsilon$  the residual concentration that can not be explained by the method. Runs were carried out for 3000 years for each models, to achieve steady state and derive the basis functions  $A_i$ .  $\lambda_i$  were obtained by minimizing the difference between  $C_{obs}$  and the right hand side of equation 11 using single value decomposition (see details in Gloor et al 2001). Regional fluxes are then given by  $F_i = \lambda_i \phi_i$ , with  $\phi_i$  the rigid flux pattern specified within each surface region of the OGCM to compute the basis function. We used the spatial pattern of Takahashi et al (2002) for CO<sub>2</sub> fluxes and the heat flux pattern of Esbensen and Kushnir (1981) for heat, O<sub>2</sub> and N<sub>2</sub> fluxes.

Basis functions ( $A_i$ ) for the MOM models are identical to those used by Jacobson et al (2007). The MITgcm-2.8 and MITgcm-ECCO basis functions were computed using the Transport Matrix Method that provides monthly mean transport matrices for 3000 years based on the climatological transport during the 1992-2004 period (Khatiwala et al 2005; Khatiwala 2007; Stammer et al 2004).

Air-sea fluxes were estimated for the 30 regions but the result usually displayed large covariance between adjacent regions (e.g. regions 13 to 15 in the North Pacific or regions 9, 25 and 30 in the subpolar Southern Ocean) showing that these fluxes estimates are not independent. To avoid this type of underdetermination, we aggregated the 30 original fluxes into 21 regional fluxes (Figure 12). Results for those 21 regions are detailed in Tables 7, 8, 9 and 10. We performed a first set of inversions without constraining the balance of the total flux. We found that this method resulted in only relatively small imbalances in the predicted fluxes (for example -0.1 to 0.1 PgC y<sup>-1</sup> for CO<sub>2pi</sub> and 30 to 50 Tmol y<sup>-1</sup> for O<sub>2</sub>), which gives us confidence that this technique is able to capture large scale regional gradients.

Ocean interior inversions incorrectly interpret the addition of carbon by rivers as an air-to-sea flux (see discussion in Gruber et al (2009) supplementary material). At steady-state, the sum of air-sea flux and river input at global scale and hence the result of our inversion has to be balanced. We therefore performed a second set of inversions using Lagrangian multipliers to enforce the constraint that the sum of global fluxes was zero (Gloor et al 2001). Only this second set is reported here.

Biogeochemical variables are sampled with lower coverage than temperature and salinity in the GLODAP dataset. We tested the impact of lower coverage by carrying out the heat inversion with both coverages: the full GLODAP dataset, i.e.  $\sim 270\,000$  data points and the biogeochemical coverage, i.e.  $\sim 80\,000$  data points. This test revealed that the heat transport asymmetry ( $A_Q$ ) only varies by about 0.02 PW when using the subset. The low sensitivity to this sub-sampling is explained by the relatively good coverage of biogeochemical sampling, roughly performed along the same transects, but with a lower spatial resolution. Only results from the subset where biogeochemical variables are available are presented here.

## C Simulated atmospheric potential oxygen computation and uncertainties

To allow comparison with atmospheric data, we combined annual inverse model air-sea fluxes with additional fluxes as follows:

$$F_O = F_{Oan} + F_{Cseas} + F_{Off} \quad (12)$$

$$F_C = F_{Cpi} + F_{Cseas} + F_{Canth} + F_{Cff} \quad (13)$$

$$F_N = F_{Nan} + F_{Nseas} \quad (14)$$

The seasonal variations are those of Garcia and Keeling (2001) for  $O_2$ , Rödenbeck et al (2013) for  $CO_2$  and based on solubility changes expected from the seasonality of heat fluxes for  $N_2$  Keeling and Shertz (1992). The seasonality of  $O_2$  was turned down by 18% following the recent results of Bent (2014) suggesting that the amplitude reported in Garcia and

Keeling (2001) was overestimated. The anthropogenic air-sea flux of CO<sub>2</sub>  $F_C^{ant}$  is from Khatiwala et al (2009) and the fossil fuel  $F_C^{ff}$  is taken from the Emission Database for Global Atmospheric Research (EDGAR, available at <http://edgar.jrc.ec.europa.eu>) and  $F_O^{ff}$  is computed by scaling  $F_C^{ff}$  using a constant stoichiometric ratio of -1.4 (Keeling 1988). To enable the comparison between model estimates, stations data and airborne data, all fluxes are referenced to year 2009 by correcting for fossil fuel using EDGAR emission database and for oceanic anthropogenic carbon uptake using Khatiwala et al (2009).

APO was estimated using Equation 8 obtained assuming there is no changes in the total moles of air and that  $(\frac{O_2}{N_2})_{reference} = \frac{X_{O_2}}{X_{N_2}}$  following Stephens et al (1998). Uncertainties on resulting APO values include uncertainties on the rectifier effect, on anthropogenic carbon fluxes, on fossil fuel burning emissions and on the atmospheric circulation. The rectifier effect is the contribution to annual mean APO due to purely seasonal fluxes. We assigned a 20% uncertainty to the seasonal rectifier effect based on the numerous studies of its dependency to both the atmospheric model used and the seasonal flux estimates (e.g. Stephens et al 1998; Blaine 2005; Battle et al 2006; Tohjima et al 2012). We used the recent estimation of the uncertainty associated with fossil fuel carbon dioxide emission by Andres et al (2014): 8.5% (2 standard deviations). We used a conservative 20% uncertainty on the anthropogenic air-sea flux of Khatiwala et al (2009). Finally, the uncertainty on  $\Delta APO$  associated with the atmospheric circulation was estimated to  $\pm 0.5$  per meg, by comparing APO fields obtained using NCEP winds vs. ERA-Interim winds (Fig 8 a).

**Table 1** Overturning circulation following Gnanadesikan (1999). Units are Sv.  $M_{North}$  is the maximum northward transport at 48°N using the meridional stream function.  $M_{South}$  is the transport across the thermocline ( $\sigma_\theta = 24.7$ ) at 32°S. The contribution of  $M_{Upwelling}$  is then deduced from the difference between  $M_N$  and  $M_{South}$ .

	MOM-HH	MOM-LHS	MOM-LL	MOM-PSS	MOM-RDS	MITgcm-2.8	MITgcm-ECCO
$M_{North}$	15.3	15.9	14.5	16.1	16.2	15.5	20.5
$M_{South}$	-8.4	4.9	3.9	11.3	2.7	2.3	12.6
$M_{Upwelling}$	23.8	11	10.6	4.8	13.5	13.2	7.9

**Table 2**  $\Delta$ APCO column along the HIPPO transect in the data, from ocean inversions, the contributions of annual mean  $O_2$  ( $O_{an}$ ),  $C_{pi}$  ( $C_{pi}$ ) and  $N_2$  ( $N_{an}$ ) from MITgcm-ECCO inversion and the contributions of fossil fuel (ff), seasonal rectifier effect (seas) and anthropogenic carbon ( $C_{anth}$ ) used in all inversions.

$\Delta$ APCO column	
HIPPO	-10.4±0.9
MOM-HH	-3.9±0.8
MOM-LHS	-5.9±0.8
MOM-LL	-6.0±0.8
MOM-PSS	-6.0±0.8
MOM-RDS	-5.2±0.8
MITgcm-2.8	-5.0±0.8
MITgcm-ECCO	-6.4±0.8
ff	-6.6±0.01
seas	-0.9±0.2
$C_{anth}$	3.4±0.1
MITgcm-ECCO $C_{pi}$	-2.4
MITgcm-ECCO $O_{an}$	<-0.1
MITgcm-ECCO $N_{an}$	0.2

**Table 3** Global ocean heat transport asymmetry between 20°S and 20°N (in PW) from hydrographic sections (Ganachaud and Wunsch 2003; Talley 2003), air-sea flux bulk formulations (Large and Yeager 2009) and top of the atmosphere budgets (Trenberth and Caron 2001; Fasullo and Trenberth 2008), the MITgcm-ECCOv1 forward simulation and our inverse calculation based on the same version of MITgcm-ECCO. Note that meridional heat transports are computed where sections are available in observations: between 24°S and 24°N for Talley (2003) and between 19°S and 24°N for Ganachaud and Wunsch (2003).

estimates	global	Atlantic	Indo-Pacific
Ganachaud and Wunsch (2003)	0.5±0.6	1±0.3	0.5±0.5
Talley (2003)	-	0.8	-
Large and Yeager (2009)	0.8±0.3	-	-
Fasullo and Trenberth (2008)	0.4	-	-
Trenberth and Caron (2001) ECMWF	0.1	-	-
Trenberth and Caron (2001) NCEP	0.5	-	-
MITgcm-ECCO forward	0.3	0.6	-0.3
MITgcm-ECCO inverse (this study)	0.2	0.5	-0.3



**Table 4** Northward heat transport (in PW) at 26°N in the Atlantic Ocean. Results from the MITgcm-ECCO forward simulation are compared to observations from the RAPID array and the Florida Straight survey (Johns et al 2008, 2011). The total meridional heat transport across the section ( $\iint_{xz} \rho c_p \times v \times \theta dx dz$ ) is broken down into the contributions of overturning ( $\int_z \rho c_p \times \bar{v} \times \bar{\theta} dz$ ) and gyre circulation ( $\iint_{xz} \rho c_p \times v^* \times \theta^* dx dz$ ).  $v$  is the meridional velocity and  $\theta$  the potential temperature. Overbars denote the zonal average across the entire transoceanic section and asteriks the deviations from this mean (Johns et al 2011).

	Observations	MITgcm-ECCO forward
Total	1.33±0.40	1.08±0.21
Gyre	-0.15±0.07	-0.05±0.05
Overturning	1.18±0.37	1.03±0.23

**Table 5** The 7 HIPPO transects used to construct the annual mean meridional transect

HIPPO campaign	Date	Research Flights (RF)
1	Jan. 2009	RF3-RF7
3	Mar. 2010	RF2-RF6
3	Apr. 2010	RF7-RF10
4	Jun. 2011	RF2-RF6
5	Aug. 2011	RF5-RF9
5	Sep. 2011	RF10-RF13
2	Nov. 2009	RF2-RF6

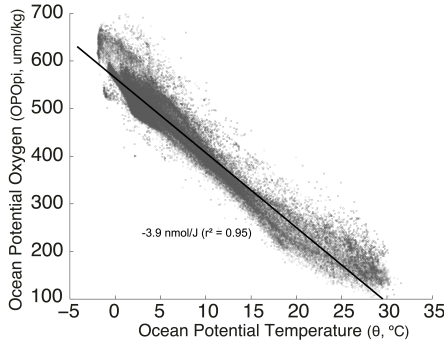


**Fig. 1** Ocean potential temperature ( $\theta$ ) vs. pre-industrial ocean potential oxygen ( $OPO_{pi}$ ) in the GLODAP dataset.  $OPO_{pi}$  is conservative with respect to the marine biosphere, removes variations associated with anthropogenic carbon using estimates from Khatiwala et al (2009) and is strongly coupled to thermal air-sea exchanges of  $O_2$  and  $CO_2$ . The slope is  $-15.6 \mu\text{mol Kg}^{-1} \text{ degC}^{-1}$ , equivalent to  $-3.9 \text{ nmol per joule of warming}$  as derived by multiplying by an average thermal capacity of  $3990 \text{ J Kg}^{-1} \text{ degC}^{-1}$ . The curvature in the slope of the data arises from non-linearities in  $O_2$  and  $CO_2$  solubilities, which are more sensitive to temperature change at lower temperature. Note however that this curvature is much smaller for  $OPO_{pi}$  than for  $O_2^*$  (Gruber et al 2001; Keeling and Garcia 2002).

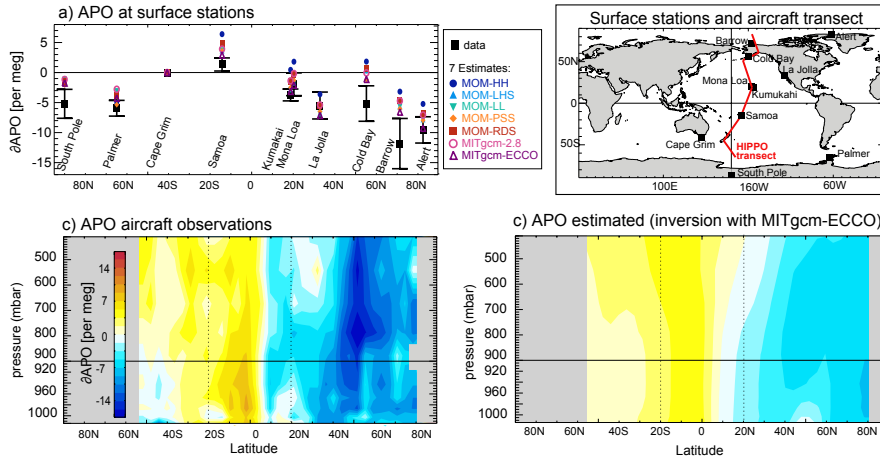


**Fig. 2** Annual mean meridional APO gradient and referenced to the value at Cape Grim station ( $\partial APO = APO - APO(\text{Cape Grim})$ , in per meg). a) Observed at Scripps surface stations (black symbols and dotted line) and estimated from inverse air-sea flux estimates using GLODAP data and 7 ocean model transports (colored symbols). b) Observed during the HIPPO aircraft campaign. c) Estimated along the HIPPO transect from inverse air-sea flux estimates using GLODAP data, MITgcm-ECCO ocean transport and TM3 atmospheric transport. Error bars on observed annual means correspond to the interannual variability at each surface station ( $\pm 1$  standard deviation). The top right insert shows the map of the 9 atmospheric Scripps surface stations (black symbols) and the approximate transect of HIPPO aircraft campaigns (red line).

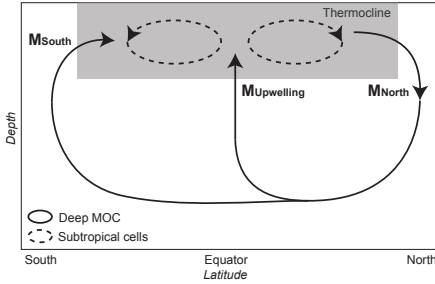


**Fig. 3** a) Schematic of the meridional circulation associated with i) the deep meridional overturning circulation (MOC) that transforms thermocline waters into deep waters and vice-versa and ii) the shallow circulation within the thermocline e.g. the subtropical cells. The main fluxes of the deep MOC described by Gnanadesikan (1999) are shown: the northern sinking flux ( $M_{North}$ ), the upwelling of deep waters in the tropical region ( $M_{Upwelling}$ ) and the balance between wind-driven upwelling and eddy-return flow in the Southern Ocean ( $M_{South}$ ). Note that  $M_{North} = M_{South} + M_{Upwelling}$ .

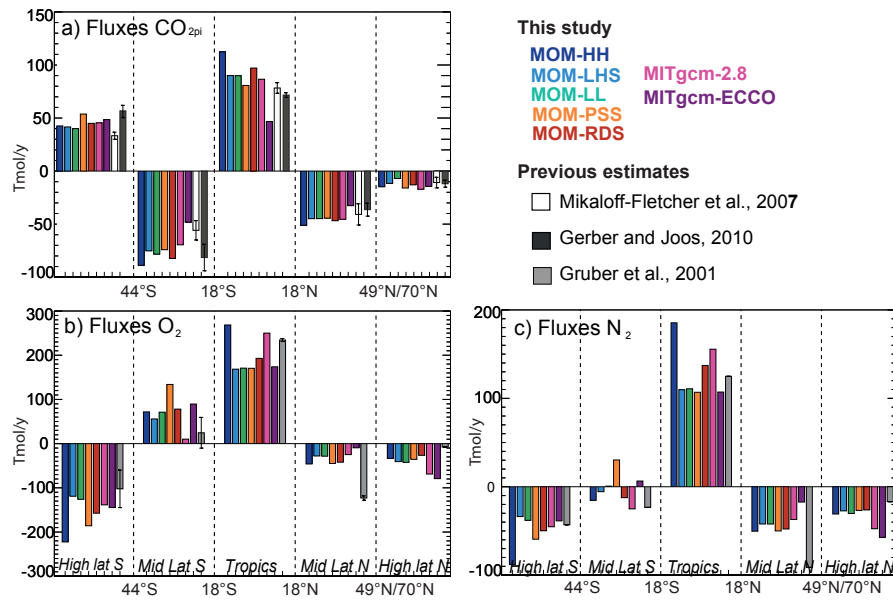


**Fig. 4** Air-sea fluxes based on ocean interior inversions for a) pre-industrial  $\text{CO}_2$ , b)  $\text{O}_2$  and c)  $\text{N}_2$ . The results obtained with the 7 OGCMs in this study (color) are compared to previous estimates (mean  $\pm 1$  standard deviation across obtained estimates): Mikaloff Fletcher et al (2007, 10 estimates) and Gerber and Joos (2010, 4 estimates) for  $\text{CO}_{2pi}$  and Gruber et al (2001, 2 estimates) for  $\text{O}_2$  and  $\text{N}_2$ . Note that the northern high-latitude region is north of  $49^\circ\text{N}$  in the Pacific and north of  $70^\circ\text{N}$  in the Atlantic.

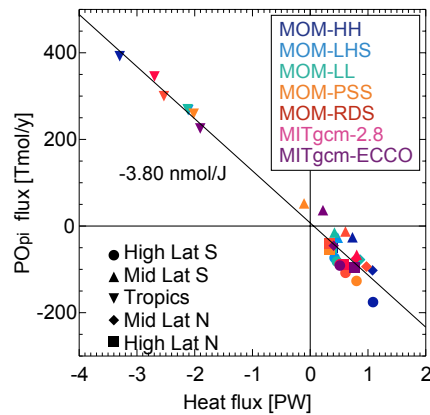


**Fig. 5** Air-sea pre-industrial potential oxygen ( $\text{PO}_{pi}$ ) flux vs. air-sea heat flux obtained from the 7 inverse estimates and for the latitudinal bands of Figure 6 a and d.

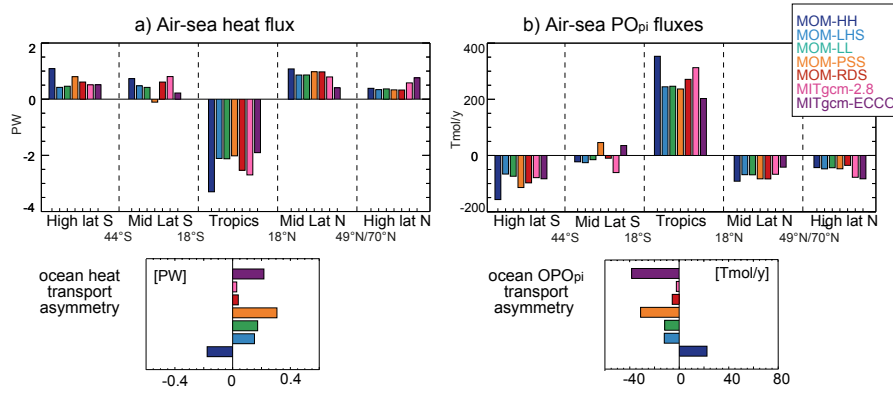


**Fig. 6** Air-sea fluxes and interhemispheric transports of a) heat and b) pre-industrial PO ( $PO_{pi}$ ).  $APO_{pi}$  fluxes are based on the 7 ocean interior inversion results shown in Fig. 4. The associated oceanic interhemispheric transports of heat and pre-industrial OPO ( $OPO_{pi}$ ) are computed as the asymmetry between  $20^\circ\text{S}$  and  $20^\circ\text{N}$ .

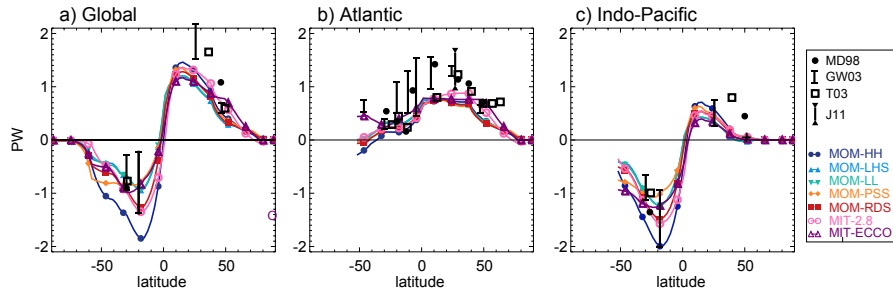


**Fig. 7** Oceanic meridional heat transport in a) the global ocean, b) the Atlantic and c) the Indo-Pacific. Transports are positive northward. Units are PW. Observations are from Macdonald (1998, MD98), Talley (2003, T03), Ganachaud and Wunsch (2003, GW03) and Johns et al (2011, J11).

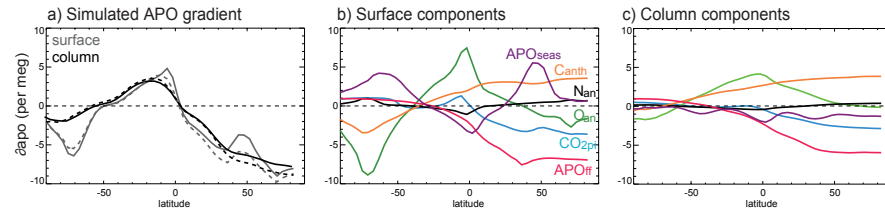


**Fig. 8** Contributions of the seasonally varying APO flux (seas), the anthropogenic carbon air-sea flux (anth) and the fossil fuel combustion (ff) are used for all inverse estimates.  $\partial APO$  is defined at each point by the difference in APO with the Cape Grim station.

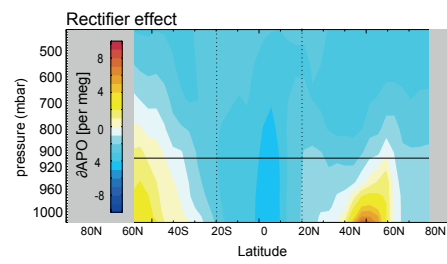


**Fig. 9** Contribution of the rectifier effect to the annual mean meridional APO gradient in the Pacific and referenced to the value at Cape Grim station ( $\partial\text{APO} = \text{APO} - \text{APO}(\text{Cape Grim})$ ), in per meg).

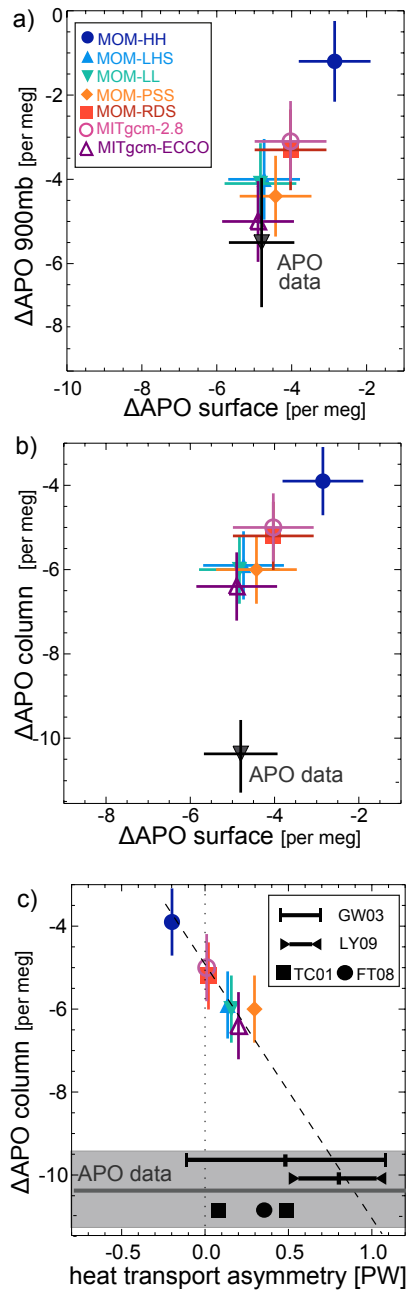


**Fig. 10** a-b) Evaluation of the northern atmospheric potential oxygen (APO) deficit using Scripps surface stations ( $\Delta\text{APO surface}$ ) compared to the airborne HIPPO transect at 900 mb ( $\Delta\text{APO 900 mb}$ ) and column averaged over the lower troposphere ( $\Delta\text{APO column}$ ). c) Relationship between the vertically integrated northern APO deficit and the meridional heat transport. Meridional heat transports from hydrographic sections (Ganachaud and Wunsch 2003, GW03), air-sea fluxes bulk formulations (Large and Yeager 2009, LY09) and top of the atmosphere budgets (Trenberth and Caron 2001; Fasullo and Trenberth 2008, TC01 and FT08) are indicated in black (see details in Table 3). Uncertainties on the observed APO deficit are related to the annual mean computation from a 1-year (15-year) time-series for HIPPO (for surface stations, see Appendix A). Error bars on inverse estimates include uncertainties from fossil fuel, anthropogenic carbon uptake, seasonal rectifier effect and atmospheric circulation (see Appendix C). All APO values are referenced to year 2009.

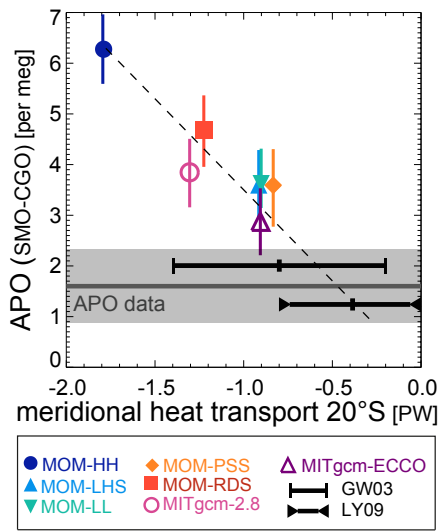


**Fig. 11** APO meridional gradient between Samoa (SMO) and Cape Grim (CGO) vs. the oceanic transport of heat at 20°S. The APO difference observed between Samoa and Cape Grim surface stations is indicated in grey. Previous estimates of heat transports at 20°S are from Ganachaud and Wunsch (2003, GW03) and Large and Yeager (2009, LY09). Uncertainties are computed as in Figure 10. APO values are referenced to year 2009.

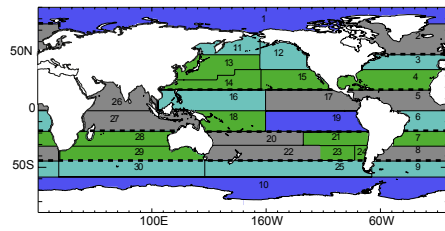


**Fig. 12** Maps of 30 regions used for the ocean interior inversion (1 to 30 separated by thin lines) and 21 regions after aggregation of adjacent regions within individual basins (colored). Thick dashed lines indicate the large regions used to compare inverse fluxes on Figure 4.

**Table 6** Comparison to previous ocean interior inversion studies

	Fluxes	Ocean models	Inversion regions*	Inversion Details
Gruber et al (2001)	O <sub>2</sub> , N <sub>2</sub>	MOM-LL	15(13)	constrained to 0 flux/unconst
Gloor et al (2003)	CO <sub>2</sub>	MOM-LL	13	unconstrained
Mikaloff Fletcher et al (2006, 2007)	CO <sub>2</sub>	10 models including MOM-LL MOM-HH, MOM-LHS, MOM-PSS MOM-RDS, MITgcm-2.8, MITgcm-ECCO	30(24)	unconstrained
Gerber and Joos (2010)	CO <sub>2</sub>	Bern3D	17(16)	32 members ensemble
This study	CO <sub>2</sub> , O <sub>2</sub> , N <sub>2</sub>	MOM-LL, MOM-HH, MOM-LHS MOM-PSS, MOM-RDS MITgcm-2.8, MITgcm-ECCO	30(21)	constrained to 0 flux

\*Number of regions used to perform the inversion and if different the number of regions retained after aggregation in parenthesis.



**Table 7** Regional air-sea heat fluxes obtained with the 7 ocean interior inversions (in PW). Region numbers in parenthesis refer to Figure 12. Positive fluxes are towards the atmosphere.

Regions	MOM-HH	MOM-LHS	MOM-LL	MOM-PSS	MOM-RDS	MITgcm-2.8	MITgcm-ECCO
High Lat N 49°N/70°N:90°N							
Arctic Ocean (1)	0.04	0.09	0.09	0.13	0.09	-0.12	-0.02
North Atlantic >49°N (2)	0.35	0.25	0.27	0.20	0.24	0.70	0.78
Mid Lat N 20°N:49°N/70°N							
North Atlantic <49°N (3)	0.33	0.33	0.32	0.32	0.35	0.29	0.00
(4)	0.05	0.09	0.10	0.09	0.08	-0.02	0.01
North Pacific <70°N (11)	0.08	0.02	0.02	0.07	0.04 0.05	0.02	
(12)	-0.03	-0.07	-0.08	-0.01	-0.04	0.02	-0.01
(13-14-15)	0.65	0.50	0.50	0.50	0.53	0.45	0.38
Tropics 20°S:20°N							
Atlantic (5)	-0.11	-0.01	-0.02	-0.08	-0.07	-0.19	0.01
(6)	-0.51	-0.46	-0.46	-0.43	-0.47	-0.44	-0.35
Pacific (16)	-0.12	0.16	0.16	0.07	0.11	-0.28	-0.18
(17)	-0.60	-0.29	-0.29	-0.58	-0.42	-0.59	-0.38
(18)	-0.18	0.00	-0.00	-0.07	-0.08	-0.13	-0.02
(19)	-1.16	-1.06	-1.07	-0.62	-1.06	-0.53	-0.52
Indian (26-27)	-0.62	-0.45	-0.45	-0.31	-0.54	-0.54	-0.47
Mid Lat S 44°S:20°S							
South Atlantic (7)	0.01	0.03	0.03	-0.01	0.03	0.03	-0.21
(8)	-0.29	-0.29	-0.31	-0.23	-0.29	-0.17	0.22
South Pacific (20-22)	0.68	0.41	0.39	0.39	0.44	0.47	0.22
(21-23-24)	-0.22	-0.26	-0.26	-0.45	-0.25	-0.24	-0.32
South Indian (28-29)	0.56	0.59	0.56	0.19	0.67	0.71	0.30
High Lat S <44°S							
Subpolar <44°S (9-25-30)	0.61	0.08	0.18	0.09	0.14	0.41	0.06
Southern Ocean <58°S (10)	0.47	0.35	0.28	0.71	0.47	0.10	0.45

**Table 8** Regional air-sea O<sub>2</sub> fluxes obtained with the 7 ocean interior inversions (in Tmol y<sup>-1</sup>). Region numbers in parenthesis refer to Figure 12. Positive fluxes are towards the atmosphere.

Regions	MOM-HH	MOM-LHS	MOM-LL	MOM-PSS	MOM-RDS	MITgcm-2.8	MITgcm-ECCO
High Lat N 49°N/70°N:90°N							
Arctic Ocean (1)	3.40	-5.60	-6.78	-7.57	-3.77	16.68	9.13
North Atlantic >49°N (2)	-41.69	-32.0262	-41.61	-20.71	-29.09	-91.66	-95.12
Mid Lat N 20°N:49°N/70°N							
North Atlantic <49°N							
(3)	-38.62	-33.20	-33.16	-28.25	-37.45	3.46	10.63
(4)	28.18	16.90	16.60	13.09	19.32	3.60	6.80
North Pacific <70°N							
(11)	-18.27	-5.15	-5.11	-16.13	-10.64	-9.41	-9.40
(12)	0.39	13.16	13.46	-4.99	3.44	-10.34	-5.17
(13-14-15)	-24.83	-33.28	-34.30	-21.84	-25.98	-15.73	-18.05
Tropics 20°S:20°N							
Atlantic							
(5)	7.64	-0.46	-0.32	6.82	4.88	18.29	13.63
(6)	46.78	37.53	38.59	35.92	41.03	48.09	23.07
Pacific							
(16)	18.31	-11.15	-12.18	5.11	-3.99	29.09	20.02
(17)	50.62	18.91	19.40	45.27	32.48	55.52	29.90
(18)	12.54	-1.71	-0.96	2.11	5.68	10.30	13.10
(19)	85.72	72.26	72.44	39.10	73.53	40.31	43.15
Indian							
(26-27)	44.89	31.66	32.07	15.30	39.38	46.37	34.17
Mid Lat S 44°S:20°S							
South Atlantic							
(7)	4.89	-0.72	-2.34	2.60	-1.59	-2.18	19.77
(8)	64.07	60.55	68.79	55.02	64.58	42.49	4.41
South Pacific							
(20-22)	-20.59	-1.46	0.52	8.50	-2.50	-20.21	10.49
(21-23-24)	33.40	37.86	35.94	57.99	41.82	28.51	40.48
South Indian							
(28-29)	-17.79	-21.18	-14.44	37.19	-32.58	-40.33	18.09
High Lat S <44°S							
Subpolar <44°S (9-25-30)	-168.07	-60.61	-69.54	-95.09	-95.52	-134.95	-74.20
Southern Ocean <58°S (10)	-68.95	-80.45	-74.72	-127.45	-81.00	-16.53	-94.02

**Table 9** Regional air-sea  $N_2$  fluxes obtained with the 7 ocean interior inversions (in  $Tmol\ y^{-1}$ ). Regions numbers in parenthesis refer to figure 12. Positive fluxes are towards the atmosphere.

Regions	MOM-HH	MOM-LHS	MOM-LL	MOM-PSS	MOM-RDS	MITgcm-2.8	MITgcm-ECCO
High Lat N 49°N/70°N:90°N							
Arctic Ocean (1)	-3.48	-7.11	-7.49	-10.49	-6.96	9.26	-0.76
North Atlantic >49°N (2)	-27.35	-20.19	-22.76	-16.29	-19.26	-56.77	-56.48
Mid Lat N 20°N:49°N/70°N							
North Atlantic <49°N (3)	-18.38	-18.66	-18.06	-16.89	-20.04	-11.08	1.59
(4)	1.62	-2.21	-2.53	-3.24	-1.35	1.87	1.31
North Pacific <70°N (11)	-7.00	-2.03	-2.04	-6.41	-4.10	-4.44	-3.91
(12)	1.13	5.22	5.30	-0.61	1.89	-3.14	-0.46
(13-14-15)	-27.69	-24.47	-24.86	-22.80	-24.19	-20.25	-15.86
Tropics 20°S:20°N							
Atlantic (5)	5.50	0.30	0.62	4.12	3.35	10.41	0.34
(6)	29.38	24.49	24.69	23.42	25.99	26.03	19.32
Pacific (16)	7.83	-8.45	-8.66	-3.56	-4.98	18.18	11.98
(17)	33.52	14.45	14.56	32.06	22.81	35.42	21.92
(18)	8.32	-1.36	-1.01	2.93	3.15	5.30	-0.65
(19)	64.35	56.51	56.67	31.05	56.87	29.16	29.20
Indian (26-27)	36.54	23.79	23.95	16.83	29.98	31.08	25.00
Mid Lat S 44°S:20°S							
South Atlantic (7)	0.72	-1.46	-1.91	0.39	-1.67	-1.57	11.72
(8)	23.31	23.23	26.30	21.43	23.31	13.77	-10.41
South Pacific (20-22)	-32.79	-19.48	-18.31	-17.64	-20.61	-23.36	-9.07
(21-23-24)	15.63	16.72	16.51	28.77	17.16	17.21	21.51
South Indian (28-29)	-22.20	-24.60	-21.90	-2.66	-30.55	-31.12	-7.30
High Lat S <44°S							
Subpolar <44°S (9-25-30)	-41.39	2.18	-6.67	14.53	-3.27	-30.42	15.75
Southern Ocean <58°S (10)	-46.60	-35.97	-31.33	-73.89	-46.55	-14.83	-54.40

**Table 10** Regional air-sea  $\text{CO}_{2pi}$  fluxes obtained with 7 ocean interior inversions and 2009 air-sea  $C_{ant}$  fluxes from Khatiwala et al (2009, KWLA09) (in  $\text{Tmol y}^{-1}$ ). Region numbers in parenthesis refer to Figure 12. Positive fluxes are towards the atmosphere.

Regions	MOM-HH	MOM-LHS	MOM-LL	MOM-PSS	MOM-RDS	MITgcm-2.8	MITgcm-ECCO	$C_{ant}$ 2009
High Lat N 49°N/70°N:90°N								
Arctic Ocean (1)	-5.13	-2.44	2.12	-7.06	-4.70	5.67	-1.54	-
North Atlantic >49°N (2)	-9.70	-9.15	-9.13	-8.91	-8.29	-22.80	-12.93	-9.1
Mid Lat N 20°N:49°N/70°N								
North Atlantic <49°N (3)	-12.60	-12.24	-11.87	-13.51	-12.37	-14.65	-17.58	-8.4
(4)	-5.92	-5.77	-5.94	-4.89	-5.75	-4.36	0.91	-7.9
North Pacific <70°N (11)	3.53	1.63	1.60	2.86	2.35	2.20	4.10	-2.4
(12)	-0.95	-3.50	-3.55	0.17	-1.72	1.45	-0.06	-4.8
(13-14-15)	-35.22	-25.00	-25.05	-29.00	-29.30	-30.05	-20.00	-14.7
Tropics 20°S:20°N								
Atlantic (5)	2.63	-0.04	0.28	1.58	1.02	6.08	-0.55	-3.1
(6)	15.29	14.52	14.03	13.29	14.08	11.41	7.68	-3.6
Pacific (16)	14.01	7.60	7.95	7.70	9.54	15.72	3.84	-5.5
(17)	5.02	5.49	5.35	12.92	5.94	4.24	1.46	-6.0
(18)	10.07	1.51	1.37	2.31	4.69	5.91	3.40	-4.3
(19)	42.00	44.30	44.33	27.96	42.16	25.92	18.76	-7.4
Indian (26-27)	23.33	16.67	16.59	14.98	19.69	17.30	12.08	-10.8
Mid Lat S 44°S:20°S								
South Atlantic (7)	-3.14	0.41	1.11	2.58	0.60	0.40	6.07	-3.7
(8)	-9.92	-12.32	-14.65	-14.40	1-4.37	-13.02	-17.95	-6.1
South Pacific (20-22)	-36.77	-27.80	-28.50	-30.10	-28.33	-30.56	-20.43	11.8
(21-23-24)	-5.30	-4.24	-3.59	-1.03	-7.48	1.23	4.44	-5.9
South Indian (28-29)	-33.71	-31.28	-32.65	31.20	-32.79	-27.53	-20.22	-15.0
High Lat S <44°S								
Subpolar <44°S (9-25-30)	42.68	24.15	23.95	40.96	36.18	48.66	42.81	-39.1
Southern Ocean <58°S (10)	-0.11	17.47	16.08	12.80	8.82	-3.20	5.68	-34.2

**Acknowledgements** This work was made possible thanks to the scientists and personnel involved in collecting the numerous atmospheric and oceanic observations used in this study. We are grateful to the groups developing the MOM and MITgcm models for providing access to their model results. We are grateful to L. Talley, C. Wunsch, J. Marshall and R. Ferrari for valuable and inspiring discussion throughout the course of this study. Laure Resplandy was

---

granted support by the Climate Program Office of the National Oceanic and Atmospheric Administration. We thank the Deutsche Klimarechenzentrum for providing computer time and more particularly Hendryk Bockelmann for the amazing technical support.

## References

- Anderson LA, Sarmiento JL (1994) Redfield ratios of remineralization determined by nutrient data analysis. *Global Biogeochemical Cycles* 8(1):65–80, DOI 10.1029/93GB03318, URL <http://onlinelibrary.wiley.com/doi/10.1029/93GB03318/abstract>
- Andres R, Boden T, Higdson D (2014) A new evaluation of the uncertainty associated with CDIAC estimates of fossil fuel carbon dioxide emission. *Tellus B* 66(0), URL <http://www.tellusb.net/index.php/tellusb/article/view/23616>
- Atkinson CP, Bryden HL, Cunningham SA, King BA (2012) Atlantic transport variability at 25°N in six hydrographic sections. *Ocean Science* 8(4):497–523, DOI 10.5194/os-8-497-2012, URL <http://www.ocean-sci.net/8/497/2012/>
- Battle M, Fletcher SM, Bender ML, Keeling RF, Manning AC, Gruber N, Tans PP, Hendricks MB, Ho DT, Simonds C, Mika R, Paplawsky B (2006) Atmospheric potential oxygen: New observations and their implications for some atmospheric and oceanic models. *Global Biogeochemical Cycles* 20(1):n/a–n/a, DOI 10.1029/2005GB002534, URL <http://dx.doi.org/10.1029/2005GB002534>
- Bent J (2014) Airborne oxygen measurements over the southern ocean as an integrated constraint of seasonal biogeochemical processes. PhD thesis, University of California San Diego, [bluemoon.ucsd.edu/publications/jonathan/Bent.Dissertation\\_FINAL.pdf](http://bluemoon.ucsd.edu/publications/jonathan/Bent.Dissertation_FINAL.pdf)
- Blaine TW (2005) Continuous Measurements of Atmospheric Ar/N<sub>2</sub> as a Tracer of Air-Sea Heat Flux: Models, Methods, and Data. Ph.D. Thesis, University of California, San Diego, La Jolla, 225 pp
- Bryden HL, Imawaki S (2001) Ocean heat transport. In: G Siedler JC, Gould J (eds) *Ocean Circulation and Climate*, vol 103, Academic Press, San Diego, CA USA, pp 455–474
- Bryden HL, King BA, McCarthy GD, McDonagh EL (2014) Impact of a 30% reduction in Atlantic meridional overturning during 2009–2010. *Ocean Science* 10(4):683–691, DOI 10.5194/os-10-683-2014, URL <http://www.ocean-sci.net/10/683/2014/>
- Capet X, Colas F, Penven P, Marchesiello P, McWilliams JC (2008) Eastern boundary subtropical upwelling systems. In: Hecht MW, Hasumi H (eds) *Eddy Resolving ocean*

- modeling, vol 117, Geophysical Monograph Series, Washington D. C., pp 131–147
- Crowley TJ (1992) North Atlantic Deep Water cools the southern hemisphere. *Paleoceanography* 7(4):489–497, DOI 10.1029/92PA01058, URL <http://dx.doi.org/10.1029/92PA01058>
- Dee DP, Uppala SM, Simmons AJ, Berrisford P, Poli P, Kobayashi S, Andrae U, Balmaseda MA, Balsamo G, Bauer P, Bechtold P, Beljaars ACM, van de Berg L, Bidlot J, Bormann N, Delsol C, Dragani R, Fuentes M, Geer AJ, Haimberger L, Healy SB, Hersbach H, Hólm EV, Isaksen L, Kallberg P, Khler M, Matricardi M, McNally AP, Monge-Sanz BM, Morcrette JJ, Park BK, Peubey C, de Rosnay P, Tavolato C, Thpaut JN, Vitart F (2011) The ERA-Interim reanalysis: configuration and performance of the data assimilation system. *Quarterly Journal of the Royal Meteorological Society* 137(656):553–597, DOI 10.1002/qj.828, URL <http://onlinelibrary.wiley.com/doi/10.1002/qj.828/abstract>
- Esbensen SK, Kushnir Y (1981) The heat budget of the global ocean: An atlas based on estimates from surface marine observations. In: *Climate Res. Inst. Rep.*, vol 29, Oregon State Univ., USA, 27pp
- Fasullo JT, Trenberth KE (2008) The annual cycle of the energy budget. Part I: Global mean and landocean exchanges. *Journal of Climate* 21:2297–2312, DOI 10.1175/2007JCLI1935.1
- Flato G, Marotzke J, Abiodun B, Braconnot P, Chou SC, Collins W, Cox P, Driouech F, Emori S, Eyring V, Forest C, Gleckler P, Guilyardi E, Jakob C, Kattsov V, Reason C, Rummukainen M (2013) Evaluation of climate models. In: Stocker TF, Qin D, Plattner GK, Tignor M, Allen SK, Boschung J, Nauels A, Xia Y, Bex V, Midgley PM (eds) *Climate Change 2013: The Physical Science Basis. Contribution of Working Group I to the Fifth Assessment Report of the Intergovernmental Panel on Climate Change*, Cambridge University Press, Cambridge, United Kingdom and New York, NY, USA.
- Fuckar NS, Xie SP, Farneti R, Maroon EA, Frierson DMW (2013) Influence of the extratropical ocean circulation on the intertropical convergence zone in an idealized coupled general circulation model. *Journal of Climate* 26:4612–4629, DOI 10.1175/JCLI-D-12-00294.1

- Ganachaud A, Wunsch C (2003) Large-scale ocean heat and freshwater transports during the world ocean circulation experiment. *Journal of Climate* 16:31,155–31,166, DOI [http://dx.doi.org/10.1175/1520-0442\(2003\)016<0696:LSOHAF>2.0.CO;2](http://dx.doi.org/10.1175/1520-0442(2003)016<0696:LSOHAF>2.0.CO;2)
- Garcia HE, Keeling RF (2001) On the global oxygen anomaly and air-sea flux. *Journal of Geophysical Research* 106(C12):31,155–31,166, DOI 10.1029/1999JC000200, URL <http://dx.doi.org/10.1029/1999JC000200>
- Gerber M, Joos F (2010) Carbon sources and sinks from an ensemble kalman filter ocean data assimilation. *Global Biogeochemical Cycles* 24(3):n/a–n/a, DOI 10.1029/2009GB003531, URL <http://dx.doi.org/10.1029/2009GB003531>
- Gloor M, Gruber N, Hughes TMC, Sarmiento JL (2001) Estimating net air-sea fluxes from ocean bulk data: Methodology and application to the heat cycle. *Global Biogeochemical Cycles* 15(4):767–782, DOI 10.1029/2000GB001301, URL <http://dx.doi.org/10.1029/2000GB001301>
- Gloor M, Gruber N, Sarmiento J, Sabine CL, Feely RA, Rödenbeck C (2003) A first estimate of present and preindustrial air-sea CO<sub>2</sub> flux patterns based on ocean interior carbon measurements and models. *Geophysical Research Letters* 30(1):10–1–10–4, DOI 10.1029/2002GL015594, URL <http://dx.doi.org/10.1029/2002GL015594>
- Gnanadesikan A (1999) A simple predictive model for the structure of the oceanic pycnocline. *Science* 283(5410):2077–2079, DOI 10.1126/science.283.5410.2077, URL <http://www.sciencemag.org/content/283/5410/2077.abstract>, <http://www.sciencemag.org/content/283/5410/2077.full.pdf>
- Gnanadesikan A, Slater RD, Gruber N, Sarmiento JL (2002) Oceanic vertical exchange and new production: a comparison between models and observations. *Deep Sea Research Part II: Topical Studies in Oceanography* 49(13):363 – 401, DOI [http://dx.doi.org/10.1016/S0967-0645\(01\)00107-2](http://dx.doi.org/10.1016/S0967-0645(01)00107-2), URL <http://www.sciencedirect.com/science/article/pii/S0967064501001072>
- Gruber N, Sarmiento JL (2002) Biogeochemical/physical interactions in elemental cycles. In: Robinson AR, McCarthy JJ, Rothschild BJ (eds) *The Sea: Biological-Physical Interactions in the Oceans*, vol 12, John Wiley and Sons, Inc., New York, USA, pp 337–399



- Gruber N, Gloor M, Fan SM, Sarmiento JL (2001) Air-sea flux of oxygen estimated from bulk data: Implications for the marine and atmospheric oxygen cycles. *Global Biogeochemical Cycles* 15(4):783–803, DOI 10.1029/2000GB001302, URL <http://dx.doi.org/10.1029/2000GB001302>
- Gruber N, Gloor M, Fletcher SEM, Doney SC, Dutkiewicz S, Follows MJ, Gerber M, Jacobson AR, Joos F, Lindsay K, Menemenlis D, Mouchet A, Müller SA, Sarmiento JL, Takahashi T (2009) Oceanic sources, sinks, and transport of atmospheric CO<sub>2</sub>. *Global Biogeochemical Cycles* 23, DOI doi:10.1029/2008GB003349
- Hall MM, Bryden HL (1982) Direct estimates and mechanisms of ocean heat transport. *Deep Sea Research* 29A(3):339 – 359, DOI 10.1016/0198-0149(82)90099-1, URL <http://www.sciencedirect.com/science/article/pii/0198014982900991>
- Ham YG, Kug JS (2012) How well do current climate models simulate two types of El Nino? *Climate Dynamics* 39(1-2):383–398, DOI 10.1007/s00382-011-1157-3, URL <http://dx.doi.org/10.1007/s00382-011-1157-3>
- Hamme C R, Keeling F R (2008) Ocean ventilation as a driver of interannual variability in atmospheric potential oxygen. *Tellus Series B, Chemical and Physical Meteorology* 60:706–717
- Hamme RC, Emerson SR (2004) The solubility of neon, nitrogen and argon in distilled water and seawater. *Deep Sea Research Part I: Oceanographic Research Papers* 51(11):1517 – 1528, DOI <http://dx.doi.org/10.1016/j.dsr.2004.06.009>, URL <http://www.sciencedirect.com/science/article/pii/S0967063704001190>
- Heimann M, Körner S (2003) The global atmospheric tracer model TM3. In: Biogeochemie MPIF (ed) Technical Report, vol 5, Max-Planck-Institut für Biogeochemie, Jena, p 131
- Jacobson AR, Mikaloff Fletcher SE, Gruber N, Sarmiento JL, Gloor M (2007) A joint atmosphere-ocean inversion for surface fluxes of carbon dioxide: 2. regional results. *Global Biogeochemical Cycles* 21(GB1020):n/a–n/a, DOI doi:10.1029/2006GB002703
- Johns WE, Beal LM, Baringer MO, Molina JR, Cunningham SA, Kanzow T, Rayner D (2008) Variability of Shallow and Deep Western Boundary Currents off the Bahamas during 200405: Results from the 26N RAPIDMOC Array. *Jour-*

- nal of Physical Oceanography 38(3):605–623, DOI 10.1175/2007JPO3791.1, URL <http://journals.ametsoc.org/doi/abs/10.1175/2007JPO3791.1>
- Johns WE, Baringer MO, Beal LM, Cunningham SA, Kanzow T, Bryden HL, Hirschi JJM, Marotzke J, Meinen CS, Shaw B, Curry R (2011) Continuous, array-based estimates of atlantic ocean heat transport at 26.5°N. Journal of Climate 24:2429–2449, DOI 10.1175/2010JCLI3997.1
- Kalnay E, Kanamitsu M, Kistler R, Collins W, Deaven D, Gandin L, Iredell M, Saha S, White G, Woollen J, Zhu Y, Leetmaa A, Reynolds R, Chelliah M, Ebisuzaki W, Higgins W, Janowiak J, Mo KC, Ropelewski C, Wang J, Jenne R, Joseph D (1996) The ncep/ncar 40-year reanalysis project. Bull Amer Meteor Soc 77:437–471, DOI 10.1175/1520-0477(1996)077<0437:TNYRP>2.0.CO;2
- Keeling R, Manning A (2014) 5.15 - studies of recent changes in atmospheric O<sub>2</sub> content. In: Holland HD, Turekian KK (eds) Treatise on Geochemistry (Second Edition), second edition edn, Elsevier, Oxford, pp 385 – 404, DOI <http://dx.doi.org/10.1016/B978-0-08-095975-7.00420-4>, URL <http://www.sciencedirect.com/science/article/pii/B9780080959757004204>
- Keeling RF (1988) Measuring correlations between atmospheric oxygen and carbon dioxide mole fractions: a preliminary study in urban air. Journal of Atmospheric Chemistry 7:153–176
- Keeling RF, Garcia HE (2002) The change in oceanic O<sub>2</sub> inventory associated with recent global warming. Proceedings of the National Academy of Sciences 99(12):7848–7853, DOI 10.1073/pnas.122154899, URL <http://www.pnas.org/content/99/12/7848.abstract>, <http://www.pnas.org/content/99/12/7848.full.pdf+html>
- Keeling RF, Shertz SR (1992) Seasonal and interannual variations in atmospheric oxygen and implications for the global carbon cycle. Nature 358(6389):723–727, DOI 10.1038/358723a0, URL <http://www.nature.com/nature/journal/v358/n6389/abs/358723a0.html>

- Keeling RF, Stephens BB, Najjar RG, Doney SC, Archer D, Heimann M (1998) Seasonal variations in the atmospheric  $O_2/N_2$  ratio in relation to the kinetics of air-sea gas exchange. *Global Biogeochemical Cycles* 12(1):141–163, DOI 10.1029/97GB02339, URL <http://dx.doi.org/10.1029/97GB02339>
- Keeling RF, Körtzinger A, Gruber N (2010) Ocean deoxygenation in a warming world. *Annual Review of Marine Science* 2(1):199–229, DOI 10.1146/annurev.marine.010908.163855, URL <http://www.annualreviews.org/doi/abs/10.1146/annurev.marine.010908.163855>
- Key RM, Kozyr A, Sabine CL, Lee K, Wanninkhof R, Bullister JL, Feely RA, Millero FJ, Mordy C, Peng TH (2004) A global ocean carbon climatology: Results from Global Data Analysis Project (GLODAP). *Global Biogeochemical Cycles* 18(4), DOI 10.1029/2004GB002247, URL <http://dx.doi.org/10.1029/2004GB002247>
- Khatiwala S (2007) A computational framework for simulation of biogeochemical tracers in the ocean. *Global Biogeochemical Cycles* 21(3):n/a–n/a, DOI 10.1029/2007GB002923, URL <http://dx.doi.org/10.1029/2007GB002923>
- Khatiwala S, Visbeck M, Cane MA (2005) Accelerated simulation of passive tracers in ocean circulation models. *Ocean Modelling* 9(1):51 – 69, DOI 10.1016/j.ocemod.2004.04.002, URL <http://www.sciencedirect.com/science/article/pii/S1463500304000307>
- Khatiwala S, Primeau F, Hall T (2009) Reconstruction of the history of anthropogenic  $CO_2$  concentrations in the ocean. *Nature* 462:346–349, DOI doi:10.1038/nature08526
- Large WG, Yeager SG (2009) The global climatology of an interannually varying air-sea flux data set. *Climate Dynamics* 33(2-3):341–364, DOI 10.1007/s00382-008-0441-3, URL [Go to ISI://WOS:000267103700013](http://go.to/ISI://WOS:000267103700013)
- Lévy M, Klein P, Tréguier AM, Iovino D, Madec G, Masson S, Takahashi K (2010) Modifications of gyre circulation by sub-mesoscale physics. *Ocean Modelling* 34:1–15, DOI doi:10.1016/j.ocemod.2010.04.001
- Li G, Xie SP (2014) Tropical biases in cmip5 multimodel ensemble: the excessive equatorial pacific cold tongue and double itcz problems. *Journal of Climate* 27:1765–1780, DOI 10.1175/JCLI-D-13-00337.1

- Lumpkin R, Speer K (2007) Global ocean meridional overturning. *J Phys Oceanogr* 37:2550–2562, DOI <http://dx.doi.org/10.1175/JPO3130.1>
- Macdonald AM (1998) The global ocean circulation: a hydrographic estimate and regional analysis. *Progress in Oceanography* 41(3):281–382, DOI 10.1016/S0079-6611(98)00020-2, URL <http://www.sciencedirect.com/science/article/pii/S0079661198000202>
- Mahlstein I, Knutti R (2011) Ocean heat transport as a cause for model uncertainty in projected arctic warming. *Journal of Climate* 24:1451–1460, DOI 10.1175/2010JCLI3713.1
- Marshall J, Adcroft A, Hill C, Perelman L, Heisey C (1997) A finite-volume, incompressible navier stokes model for studies of the ocean on parallel computers. *Journal of Geophysical Research: Oceans* 102(C3):5753–5766, DOI 10.1029/96JC02775, URL <http://dx.doi.org/10.1029/96JC02775>
- Marshall J, Donohoe A, Ferreira D, McGee D (2014) The oceans role in setting the mean position of the Inter-Tropical Convergence Zone. *Climate Dynamics* 42(7-8):1967–1979, DOI 10.1007/s00382-013-1767-z, URL <http://dx.doi.org/10.1007/s00382-013-1767-z>
- Mazloff MR, Ferrari R, Schneider T (2013) The force balance of the southern ocean meridional overturning circulation. *Journal of Physical Oceanography* 43:1193–1208, DOI doi:10.1038/ngeo1193
- Mikaloff Fletcher SE, Gruber N, Jacobson AR, Doney SC, Dutkiewicz S, Gerber M, Follows M, Joos F, Lindsay K, Menemenlis D, Mouchet A, Mueller SA, Sarmiento JL (2006) Inverse estimates of anthropogenic CO<sub>2</sub> uptake, transport, and storage by the ocean. *Global Biogeochemical Cycles* 20(2), DOI 10.1029/2005GB002530, URL <http://dx.doi.org/10.1029/2005GB002530>
- Mikaloff Fletcher SE, Gruber N, Jacobson AR, Gloor M, Doney SC, Dutkiewicz S, Gerber M, Follows M, Joos F, Lindsay K, Menemenlis D, Mouchet A, Müller SA, Sarmiento JL (2007) Inverse estimates of the oceanic sources and sinks of natural CO<sub>2</sub> and the implied oceanic carbon transport. *Global Biogeochemical Cycles* 21(1), DOI 10.1029/2006GB002751, URL <http://dx.doi.org/10.1029/2006GB002751>
- Millero FJ, Perron G, Desnoyers JE (1973) Heat capacity of seawater solutions from 5° to 35°C and 0.5 to 22 permil chlorinity. *Journal of Geophysical Research* 78(21):4499–4507,

- DOI 10.1029/JC078i021p04499, URL <http://dx.doi.org/10.1029/JC078i021p04499>
- Nevison CD, Mahowald NM, Doney SC, Lima ID, Cassar N (2008) Impact of variable air-sea  $O_2$  and  $CO_2$  fluxes on atmospheric potential oxygen (apo) and land-ocean carbon sink partitioning. *Biogeosciences* 5(3):875–889, DOI 10.5194/bg-5-875-2008, URL <http://www.biogeosciences.net/5/875/2008/>
- Palter JB, Sarmiento JL, Gnanadesikan A, Simeon J, Slater RD (2010) Fueling export production: nutrient return pathways from the deep ocean and their dependence on the Meridional Overturning Circulation. *Biogeosciences* 7(11):3549–3568, DOI 10.5194/bg-7-3549-2010, URL <http://www.biogeosciences.net/7/3549/2010/>
- Philander SGH, Gu D, Lambert G, Li T, Halpern D, Lau NC, Pacanowski RC (1996) Why the ITCZ is mostly north of the equator. *Journal of Climate* 9(5):2958–2972, DOI 10.1175/1520-0442(1996)009<2958:WTIIMN>2.0.CO;2
- Resplandy L, Lévy M, Madec G, Pous S, Aumont O, Kumar D (2011) Contribution of mesoscale processes to nutrient budgets in the Arabian Sea. *Journal of Geophysical Research* 116(C11007), DOI doi:10.1029/2011JC007006
- Rhein M, Rintoul SR, Aoki S, Campos E, Chambers D, Feely RA, Gulev S, Johnson GC, Josey SA, Kostianoy A, Mauritzen C, Roemmich D, Talley LD, Wang F (2013) Observations: Ocean. In: Stocker TF, Qin D, Plattner GK, Tignor M, Allen SK, Boschung J, Nauels A, Xia Y, Bex V, Midgley PM (eds) *Climate Change 2013: The Physical Science Basis. Contribution of Working Group I to the Fifth Assessment Report of the Intergovernmental Panel on Climate Change*, Cambridge University Press, Cambridge, United Kingdom and New York, NY, USA.
- Rödenbeck C, Keeling RF, Bakker DCE, Metzl N, Olsen A, Sabine C, Heimann M (2013) Global surface-ocean  $pCO_2$  and sea-air  $CO_2$  flux variability from an observation-driven ocean mixed-layer scheme. *Ocean Science* 9(2):193–216, DOI 10.5194/os-9-193-2013, URL <http://www.ocean-sci.net/9/193/2013/>
- Schneider T, Bischoff T, Haug GH (2014) Migrations and dynamics of the intertropical convergence zone. *Nature* 513:45–53, DOI 10.1038/nature13636

- Severinghaus JP (1995) Studies of the terrestrial  $\text{O}_2$  and carbon cycles in sand dune gases and in biosphere 2. In: Ph.D. thesis, Columbia Univ., New York, USA
- Stammer D, Ueyoshi K, Köhl A, Large WG, Josey SA, Wunsch C (2004) Estimating air-sea fluxes of heat, freshwater, and momentum through global ocean data assimilation. *Journal of Geophysical Research* 109(C5):n/a–n/a, DOI 10.1029/2003JC002082, URL <http://dx.doi.org/10.1029/2003JC002082>
- Stephens BB, Keeling RF, Heimann M, Six KD, Murnane R, Caldeira K (1998) Testing global ocean carbon cycle models using measurements of atmospheric  $\text{O}_2$  and  $\text{CO}_2$  concentration. *Global Biogeochemical Cycles* 12(2):213–230, DOI 10.1029/97GB03500, URL <http://dx.doi.org/10.1029/97GB03500>
- Takahashi T, Sutherland SC, Sweeney C, Poisson A, Metzl N, Tilbrook B, Bates N, Wanninkhof R, Feely RA, Sabine C, Olafsson J, Nojiri Y (2002) Global sea-air  $\text{CO}_2$  flux based on climatological surface ocean  $\text{pCO}_2$ , and seasonal biological and temperature effects. *Deep Sea Research Part II: Topical Studies in Oceanography* 49(9-10):1601 – 1622, DOI 10.1016/S0967-0645(02)00003-6, URL <http://www.sciencedirect.com/science/article/B6VGC-452W7KK-2/2/cf337375806e31b8c4579d8e5d9a98c7>, the Southern Ocean I: Climatic Changes in the Cycle of Carbon in the Southern Ocean
- Talley LD (2003) Shallow, Intermediate, and Deep Overturning Components of the Global Heat Budget. *Journal of Physical Oceanography* 33(3):530–560, DOI 10.1175/1520-0485(2003)033<0530:SIADOC>2.0.CO;2
- Talley LD (2008) Freshwater transport estimates and the global overturning circulation: Shallow, deep and throughflow components. *Progress in Oceanography* 78(4):257 – 303, DOI <http://dx.doi.org/10.1016/j.pocean.2008.05.001>, URL <http://www.sciencedirect.com/science/article/pii/S0079661108001080>
- Thomas L, Ferrari R (2008) Friction, frontogenesis, frontal instabilities and the stratification of the ocean surface mixed layer. *Journal of Physical Oceanography* 38:2501–2518
- Thomas MD, Zhai X (2013) Eddy-induced variability of the meridional overturning circulation in a model of the north atlantic. *Geophysical Research Letters* 40(11):2742–2747,

- DOI 10.1002/grl.50532, URL <http://dx.doi.org/10.1002/grl.50532>
- Tohjima Y, Mukai H, Machida T, Nojiri Y, Gloor M (2005) First measurements of the latitudinal atmospheric O<sub>2</sub> and CO<sub>2</sub> distributions across the western Pacific. *Geophysical Research Letters* 32(17):n/a–n/a, DOI 10.1029/2005GL023311, URL <http://dx.doi.org/10.1029/2005GL023311>
- Tohjima Y, Minejima C, Mukai H, Machida T, Yamagishi H, Nojiri Y (2012) Analysis of seasonality and annual mean distribution of atmospheric potential oxygen (APO) in the Pacific region. *Global Biogeochemical Cycles* 26(4):n/a–n/a, DOI 10.1029/2011GB004110
- Trenberth KE, Caron JM (2001) Estimates of meridional atmosphere and ocean heat transports. *Journal of Climate* 14:3433–3443, DOI 10.1175/1520-0442(2001)014<3433:EOMAAO>2.0.CO;2
- Trenberth KE, Fasullo JT (2008) An observational estimate of inferred ocean energy divergence. *Journal of Physical Oceanography* 38:984–999, DOI 10.1175/2007JPO3833.1
- Wofsy SC, the HIPPO Science Team and Cooperating Modellers and Satellite Teams (2011) HIAPER Pole-to-Pole Observations (HIPPO): fine-grained, global-scale measurements of climatically important atmospheric gases and aerosols. *Philosophical Transactions of the Royal Society A: Mathematical, Physical and Engineering Sciences* 369(1643):2073–2086, DOI 10.1098/rsta.2010.0313, URL <http://rsta.royalsocietypublishing.org/cgi/doi/10.1098/rsta.2010.0313>
- Wofsy SC, Daube BC, Jimenez R, Kort E, Pittman JV, Park S, Commane R, Xiang B, Santoni G, Jacob D, Fisher J, Pickett-Heaps C, Wang H, Wecht K, Wang QQ, Stephens BB, Shertz S, Watt A, Romashkin P, Campos T, Haggerty J, Cooper WA, DRogers, Beaton S, Hendershot R, Elkins JW, Fahey DW, Gao RS, Moore F, Montzka SA, Schwarz JP, Perring AE, Hurst D, Miller BR, Sweeney C, Oltmans S, Nance D, Hints E, Dutton G, Watts LA, Spackman JR, Rosenlof KH, Ray EA, Hall B, Zondlo MA, Diao M, Keeling R, Bent J, Atlas EL, Lueb R, Mahoney MJ (2012) Hippo merged 10-second meteorology, atmospheric chemistry, aerosol data (r\_20121129). DOI 10.3334/CDIAC/hippo.010, carbon Dioxide Information Analysis Center, Oak Ridge National Laboratory, Oak Ridge, Tennessee, USA

- 
- Wunsch C, Heimbach P, Ponte RM, Fukumori I, the ECCO-GODAE Consortium Members  
(2009) The global general circulation of the ocean estimated by the ecco-consortium.  
Oceanography 22(2):88–103, DOI /10.5670/oceanog.2009.41
- Zhang Z, Wang W, Qiu B (2014) Oceanic mass transport by mesoscale eddies. Science  
345(6194):322–324, DOI 10.1126/science.1252418